Review | Received 21 September 2024; Accepted 5 February 2025; Published 10 February 2025
https://doi.org/10.55092/neuroelectronics20250002

Implantable imaging and photostimulation devices for biomedical applications

Yasumi Ohta[1], Virgil Christian Garcia Castillo[1], Romeo Rebusi Jr[2], Latiful Akbar[2], Joshua Philippe Olorocisimo[2], Austin Ganaway[3], Masahiro Ohsawa[4], Yasemin M. Akay[3], Metin Akay[3], Ryo Sasaki[5], Hirotaka Onoe[6], Kaoru Isa[7], Tadashi Isa[7], Yoshinori Sunaga[1], Ryoma Okada[2], Hironari Takehara[8], Kiyotaka Sasagawa[2] and Jun Ohta[1,*]

1 Institute for Research Initiatives, Nara Institute of Science and Technology, Nara, Japan
2 Graduate School of Science and Technology, Nara Institute of Science and Technology, Nara, Japan
3 Department of Biomedical Engineering, Cullen College of Engineering, University of Houston, Houston, TX, USA
4 Faculty of Pharmaceutical Science, Teikyo University, Tokyo, Japan
5 Department of System Neuroscience, National Institute for Physiological Sciences, The National Institutes of Natural Sciences, Aichi, Japan
6 Laboratory of Neuropsychopharmacology, Faculty of Pharmaceutical Sciences, Kobe Gakuin University, Hyogo, Japan
7 Department of Neuroscience, Graduate School of Medicine, Kyoto University, Kyoto, Japan
8 Nara Advanced Imaging Technology, Co., Ltd., Nara, Japan

* Correspondence author; E-mail:ohta@ms.naist.jp.

Highlights:

- Light-Based Precision in Neuroscience – Optogenetic techniques enable real-time, neuron-specific measurement and control, surpassing traditional electrical and chemical methods.
- Next-Generation Brain Implants – Active optoelectronic semiconductor devices offer miniaturization, multifunctionality, and enhanced imaging and stimulation capabilities.
- Toward a Future of "Photoceuticals" – Integrating optical diagnosis and treatment through implanted devices paves the way for groundbreaking advancements in medicine and neuroscience.

Abstract: Unlike traditional methods that implant passive optical components like fibers and rod lenses, optoelectronic semiconductor-based devices directly implant active optoelectronic semiconductors into the brain. This approach offers several advantages—the devices are compact and lightweight, enabling measurement and control without hindering the movement of small animals like mice. Additionally, it allows for simultaneous implantation of multiple devices, and integration with

other functions. However, potential temperature increment and biocompatibility due to the active nature of these devices are major drawbacks. This paper reviews novel optoelectronic semiconductor-based devices for measuring and controlling brain nerve function. The advantages of brain-implantable optoelectronic semiconductor devices for fluorescence imaging and photostimulation are highlighted. We address potential limitations and propose future improvements, demonstrating their significant potential to advance neuroscience and pharmacology.

Keywords: CMOS image sensors; implantable imaging devices; fluorescence imaging; light emitting devices; photostimulation; optogenetics; neurotransmitters; electroceuticals; photoceuticals

1. Introduction

Genetic engineering advancements now allow for the measurement and control of neurons using light. Optogenetic techniques enable the expression of light-responsive proteins like GCaMP [1], a calcium ion sensor, and ChR2 [2], a photoactivatable ion channel, in specific neuron cells, allowing for precise measurement and control using light [3,4]. Achieving such specificity with electricity is challenging, highlighting the advantage of light-based methods. While chemical methods like microdialysis [5] can measure neurotransmitters specifically, they struggle with real-time measurements. These neuron-specific, light-based techniques hold promise in neuroscience, pharmacology, and medicine.

In such applications, it is often necessary to measure and control brain function in small animals, such as mice, while they are freely behaving. This involves detecting fluorescence in the brain or introducing light into the brain, typically by inserting optical fibers [6,7]. Alternatively, fluorescence can be measured as 2D images using rod lenses (graded index (GRIN) lenses) [8,9]. Recently, a method of directly implanting active optoelectronic semiconductor devices, like ultracompact complementary metal–oxide–semiconductor (CMOS) image sensors and light-emitting diodes (LEDs) has been proposed and demonstrated [10,11]. This method offers miniaturization, weight reduction, higher performance, and multifunctionality compared to passive device implantation. Additionally, active devices can cover a wider imaging and stimulation range than passive devices.

However, these active devices generate heat, necessitating thermal management. Their varied materials require biocompatibility considerations. Exposure to electrical voltage poses electrolysis risks in contact with tissue fluid, predominantly water, necessitating embedding in a high gas barrier material to prevent water ingress.

This paper presents a case study of passive devices, such as optical fibers, implanted in the mouse brain for fluorescence imaging. It then introduces a case study on active optoelectronic semiconductor devices implanted in the mouse brain for fluorescence imaging, comparing their characteristics and issues with the passive fluorescence imaging devices. Additionally, photostimulation devices, similar to both passive and active devices, are discussed. Representative reports on active optoelectronic semiconductor devices for brain implantation are reviewed, highlighting their advantages for fluorescence imaging and photostimulation.

The use of active optoelectronic semiconductor devices implanted in the brain for measuring and controlling biological functions holds promise for advancements in neuroscience, pharmacology, and medicine. From an optical diagnosis and treatment perspective, the development of "photoceuticals," which integrates optical diagnosis and treatment with implanted active optoelectronic devices, is

explored [12]. Finally, the paper summarizes the applications of these active devices in the brain and discusses potential future directions.

2. Implantable devices for fluorescence imaging and photostimulation in the brain that enable free movement

This section describes the current status of (1) implantable devices for fluorescence imaging of the brain and (2) implantable devices for photostimulation of the brain.

2.1. Brain fluorescence imaging devices

Brain fluorescence imaging devices encompass optical fibers, head-mounted miniature fluorescence microscopes, and brain-implantable ultracompact CMOS imaging devices. Figure 1 illustrates their structures and characteristics. The optical fiber and head-mounted miniature microscope are passive devices implanted in the brain, whereas the CMOS imaging device is an active brain implant.

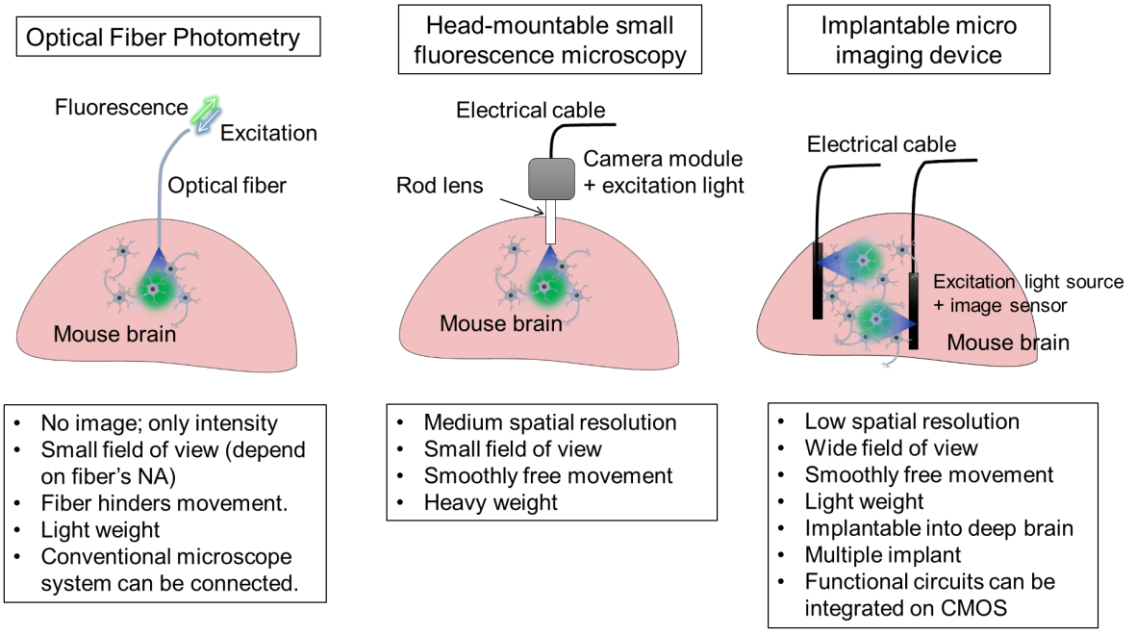

Figure 1. Concept and features of brain-implantable fluorescence imaging devices.

The optical fiber method is the simplest of the three. By inserting optical fibers into the brain, excitation light can be introduced, and fluorescence detected using a single optical fiber, known as optical fiber photometry, which is popular for its simplicity [5,6]. Ordinary optical fibers can measure fluorescence intensity near the tip but not obtain fluorescent images. For imaging, an optical fiber bundle (image fiber) is used [13]. While optical fibers are flexible, image fibers are harder to bend and have a larger diameter, making them more invasive and restricting the movement of small animals like mice. Plastic optical fibers, which are lighter and more flexible than silica glass fibers, have a loss factor that is more than two orders of magnitude higher than silica glass fibers [14]. Therefore, care is needed when using relatively long optical fibers, for example in experiments where mice are allowed to move freely.

A system using a GRIN lens instead of an image fiber has been reported; in this case, the GRIN lens is connected to the image fiber [15]. The GRIN lens bends light by varying the refractive index in a

parabolic shape from the central axis to the periphery of the glass, achieving the imaging effect of a conventional lens, and providing clearer fluorescent images than image fibers. The one end of an image fiber is connected to a GRIN lens and the other end is connected to a fluorescence microscope for imaging.

The GRIN lens method solves the problem of the optical fiber method in which image fibers restrict the free movement of mice and other animals. In this method, a super-compact fluorescence microscope device that can be attached to the head of a mouse is used to obtain fluorescence images [8, 9]. The GRIN lens projects the image onto a CMOS image sensor mounted on the head to obtain a fluorescent image. In this system, the output is an electrical signal; therefore, unlike image fibers, it is a flexible electrical cable that does not interfere with the free movement of the mice.

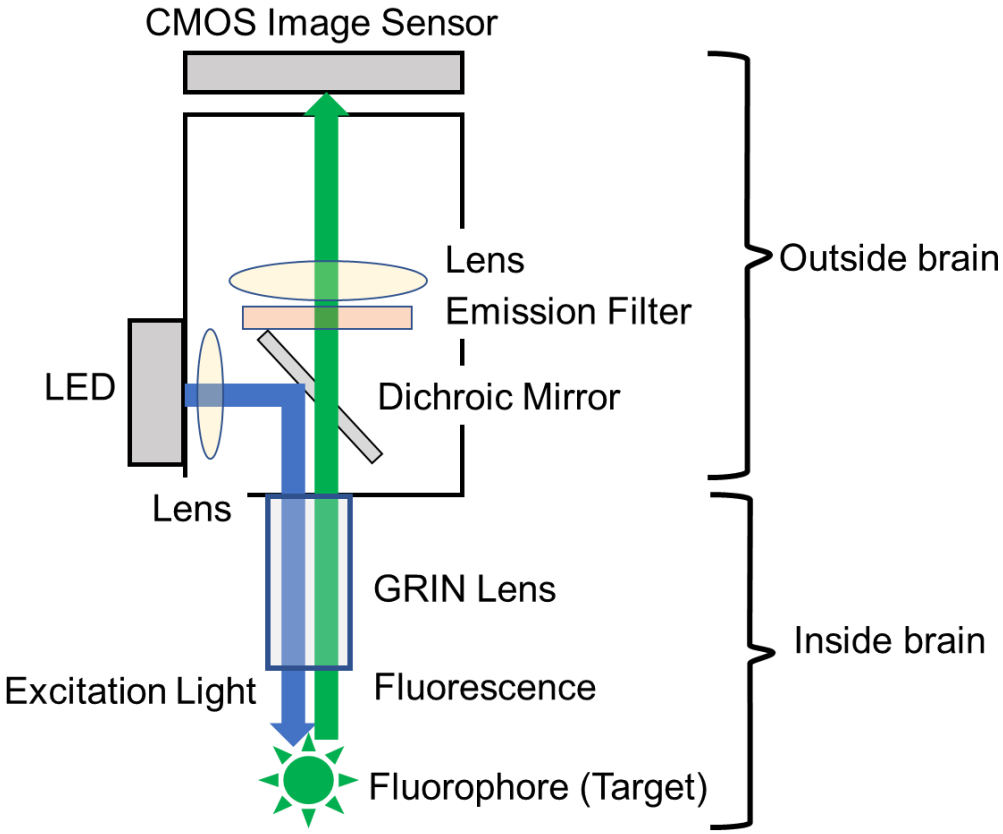

Figure 2. Structure of the head-mountable small fluorescence microscope. It mainly consists of a CMOS image sensor to detect fluorescence images, an LED as an excitation light source, and a GRIN lens to image a fluorescent target object (fluorophore). A dichroic mirror passes the fluorescence signal but rejects the excitation light. An emission filter only passes the fluorescence signal and rejects the excitation light. Drawn based on [9].

As shown in Figure 2, the head-mounted unit was equipped with an LED for excitation and the fluorescence was emitted through the GRIN lens. The head-mounted ultracompact fluorescence microscope includes a CMOS image sensor, an LED as the excitation light source, optical filters, lenses, and other optical components [9]. A GRIN lens, inserted into the brain, connects to the optical system in the head-mounted unit, enabling cellular-level activity measurement. However, with a typical diameter of ~0.5 mm [9], the lens can damage brain tissue, and the head-mounted unit's weight, approximately 2 g [9], burdens adult mice which has an average weight of 20-30g [16]. Additionally,

simultaneous measurement at multiple locations is limited to areas distant from the unit to avoid obstruction. Furthermore, similar to the optical fiber method using image fibers, the FOV (Field of View) is proportional to the GRIN lens diameter; increasing the FOV requires a larger diameter of the lens, causing more brain damage.

Both the optical fiber and GRIN lens methods involve inserting passive devices such as optical fibers, image fibers, or GRIN lenses into the brain. The CMOS device method involves the direct implantation of an active device, an image sensor, into the brain [10], [11]. This method has minimal impact on the behavior of small animals such as mice. This is because the connection is an electrical cable, as in the GRIN method, which is more flexible than optical fiber, and also because it is lighter in weight. Moreover, because the sensor is small, it is possible to implant two simultaneously. Because an image sensor is an active device with a flat shape, its FOV is proportional to its area; therefore, it can have a larger FOV with less damage than passive devices. Other advantages of the active device implantation method include the ease of integration with other functions, such as electrodes on the image sensor.

Implantable active devices face three primary issues, the first being heat generation. An increase in tissue temperature below 2°C generally does not affect cell functions [17,18]. Active devices produce heat when powered, necessitating control of this heat generation. Effective strategies include designing to minimize the device's overall power consumption and using pulse driving to manage heat output.

The second issue is the effects on and from body tissues. This is suitable for passive devices that are mainly made of glass. However, for active devices, it may be necessary to cover the surface with a biocompatible thin film, depending on the constituent elements. In addition, if water in the biological environment enters the interior of the active device, electrolysis may occur near the wiring where the voltage is applied and problems may occur during device operation owing to bubbling or pH changes. Therefore, it is necessary to protect the entire device with a film that has good gas barrier properties against water vapor. Parylene C is often used as a thin-film material because of its biocompatibility and excellent gas barrier properties [19]. Parylene C is a suitable encapsulation material for image sensors because it is transparent and has excellent electrical insulation properties.

The third issue is the detection of weak fluorescence under excitation. In fluorescence imaging, the target is irradiated with an excitation light, and only the fluorescence from the target is detected. It is necessary to detect a weak fluorescence under excitation light. In a normal fluorescence microscope, where passive devices such as optical and image fibers are connected, the excitation light is suppressed using a narrow-band optical bandpass filter (interference filter). The same is true for the mouse head-mounted fluorescence microscopy system shown in Figure 2 [9]. However, it is difficult to remove the excitation light even if such an interference filter is mounted on an implantable image sensor. This is because the interference filter allows some of the fluorescence to enter at an angle [20]. In a normal fluorescence microscope, both the excitation light and fluorescence are in the same optical path, or a coaxial configuration. Using a coaxial optical system, only the vertically incident component of the excitation light scattered by the biological tissue enters the image sensor, as shown in Figure 2. This vertically incident component of the excitation light can be suppressed using a high-performance interference filter (bandpass filter) installed in front of the image sensor. In contrast, in the implantable image sensor device, as shown in Figure 4(c), the image sensor and the LED excitation light source are not arranged in a coaxial configuration but are placed on the same plane. Therefore, the LED excitation light scattered by the biological tissue enters the image sensor from various directions.

Three methods were proposed to address this issue. The first involves using an absorption filter instead of an interference filter [10]. Absorption filters are suitable because they absorb light above a certain wavelength irrespective of the incident light's direction. However, steeply increasing the absorption spectrum is challenging, making it hard to completely suppress excitation light [21]. This issue can be mitigated by taking the difference between the current image and the reference image, if the image sensor is not saturated. The second employs pulsed excitation light, starting imaging immediately after the excitation light is turned off. Reports suggest using SPAD (Single Photon Avalanche Diode) image sensors that can respond in under 10^{-9} s [11], enabling fluorescence detection without an excitation light-cut filter. However, due to the complex signal processing circuitry of SPADs, reducing power consumption is crucial. The basic concept was validated [11], and further advancements are anticipated. In the third, a photogate controls the potential within the light-receiving element [22]. Requiring two images hinders real-time performance, and the challenge is to accurately calculate weak fluorescence. Efforts are underway to demonstrate this principle in dry environments [22], with further progress expected. Currently, the only device that has successfully recorded neural activity via fluorescence in the mouse brain, addressing these issues, uses a CMOS image sensor with an absorption filter [10].

2.2. Devices for optical brain stimulation

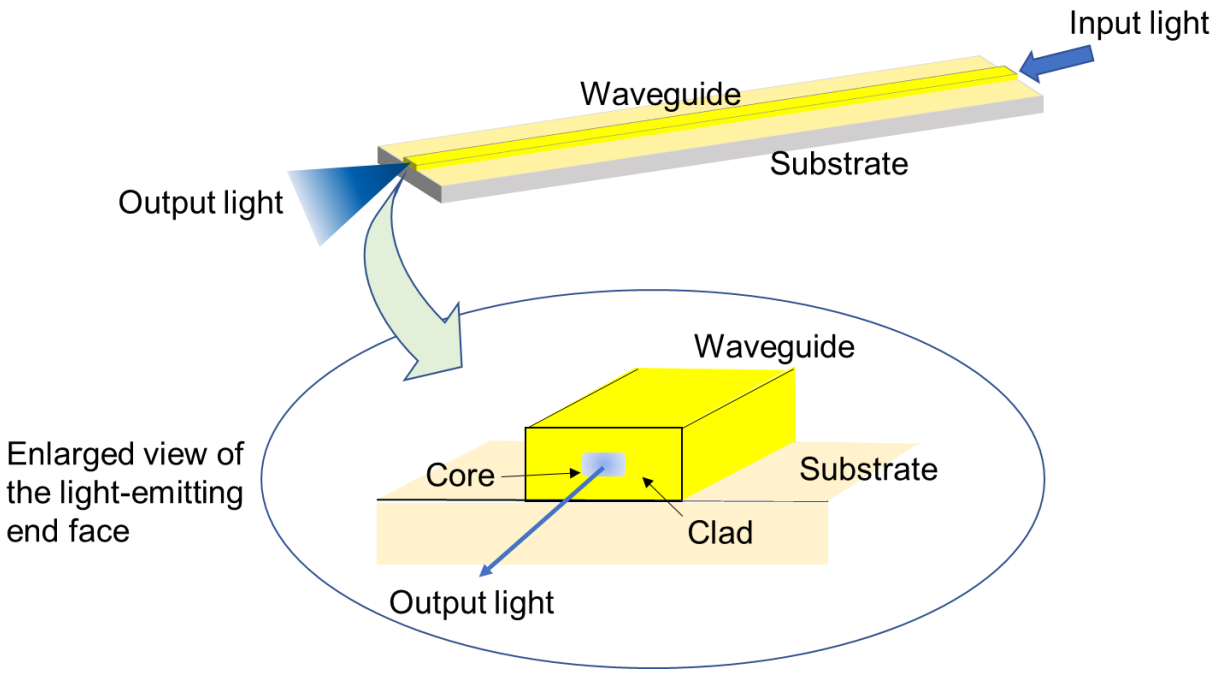

Figure 3. Optical waveguide devices.

Light typically has minimal impact on living organisms, but optogenetic technology enables the control of biological functions using light. Optogenetics manipulates cell activity by expressing light-sensitive ion channel proteins in neural cells [23]. It is widely used in neuroscience and has potential medical applications [23]. Light-sensitive proteins include excitatory ion channels like ChR2 [2] and ChrimsonR [24] and inhibitory chloride pumps like halorhodopsin [25] and JAWS [26]. Key attributes of these proteins are response speed, sensitivity, and excitation wavelength. A photostimulation device

activates cells expressing these proteins by irradiating them with light, necessitating appropriate response speed, light intensity, and emission wavelength.

Similar to the fluorescent imaging devices in Section 2.1, photostimulation devices enabling free movement are categorized into passive and active types. The passive type is popular due to its use of optical fibers, ease of use, and compatibility with existing light sources. However, light irradiation is confined to the vicinity of the optical fiber's end face, making them unsuitable for wide-area stimulation [27]. Additionally, interference between optical fibers hinders photostimulation at multiple close points smaller than the fiber's diameter.

The waveguide-type passive PS device shown in Figure 3 is compact, capable of forming multiple waveguides [28], and can emit light perpendicular to the substrate surface [29]. Furthermore, the integration of electrodes has also been reported [18]. Various active PS devices using LEDs have been reported [30–34]. The fact that it is connected by an electrical cable, which makes it easier for the animal to move freely, is also an advantage compared to passive devices. Multiple LEDs allow flexible and large light irradiation areas and enable 2D array control of photostimulation. These devices are particularly suitable for implantation in large animal brains, such as monkeys [30]. They are also easily integrated with other modalities. For instance, an integrated device with an electrocorticogram (ECoG) array in a monkey's brain has been documented [35,36]. These devices share issues with implantable fluorescence imaging devices, such as heat generation and encapsulation. LEDs produce heat, so the drive pulse pattern must be designed to prevent tissue damage. Using Parylene C as an encapsulation material ensures biocompatibility and provides a high gas barrier [19].

3. Implantable fluorescence imaging devices; i-CIS device

This section reviews implantable active devices, a type of fluorescence imaging device discussed in Section 2.1., covering their benefits and challenges. We describe an ultracompact CMOS imaging device for GCaMP that can detect intracellular calcium ion level changes during neuronal excitation and express as fluorescence changes.

3.1. Structure and features of the i-CIS device

A needle-shaped implantable CMOS imaging sensor (*i*-CIS device) can be implanted deep into the brain [10,37-39]. Table 1 lists the *i*-CIS device specifications. The *i*-CIS device, fabricated using a 0.35 μm standard CMOS process, has two imaging-area sizes: 40 × 120 and 40 × 90 pixels. Each pixel measures 7.5 × 7.5 μm^2, resulting in imaging areas of 300 × 900 and 300 × 675 μm^2.

The *i*-CIS device structure is detailed in [37]. It comprises a CMOS image sensor chip and one or two μ-LEDs on a flexible polyimide printed circuit (FPC), as illustrated in Figure 4(a). One variant features a 300-μm length from the imaging-area edge to the tip, ideal for deep brain observation. Another variant has μ-LEDs on both sides of the imaging area, enabling less biased excitation. The ultracompact device measures 680 μm in width, 225 μm in thickness, and weighs 0.02 g. It is coated with biocompatible, waterproof parylene film, which is transparent and insulating. This design allows the *i*-CIS device to be implanted in the mouse brain with minimal damage and without affecting the mouse's behavior during imaging. Figure 4(b) displays the *i*-CIS with LEDs on both sides activated, and Figure 4(c) shows its cross-sectional structure when implanted in the brain and neurons.

Table 1. Specifications of the image sensor.

Chip size	450 μm×1568 μm	450 μm×1333 μm
Pixel number	40×120	40×90
Image area size	300 μm×900 μm	300 μm×675 μm
Fill factor	44%	
Pixel structure	3T-APS	
Technology	TSMC 0.35 μm standard CMOS 2-poly-4-metal process	

The *i*-CIS device uses a 470 nm μ-LED for targeting GFP, like GCaMP, and includes an absorption filter to block blue LED light while transmitting GFP's green light. Figure 4(d) illustrates the spectral characteristics of the blue LED's excitation, GFP fluorescence, and the filter's transmission properties, showing some LED light leakage through the filter due to its gradual increase. Consequently, the GCaMP fluorescence image in *i*-CIS is overlaid with this leakage light as background. To address this, *i*-CIS device employs differential imaging to eliminate the background leakage. However, if the leaked excitation light is intense, then it can saturate the sensor output, rendering the differential processing ineffective and preventing the acquisition of a clear fluorescent image, especially for pixels near the LED. This limitation is a drawback compared to the filterless devices discussed in Section 2.1.

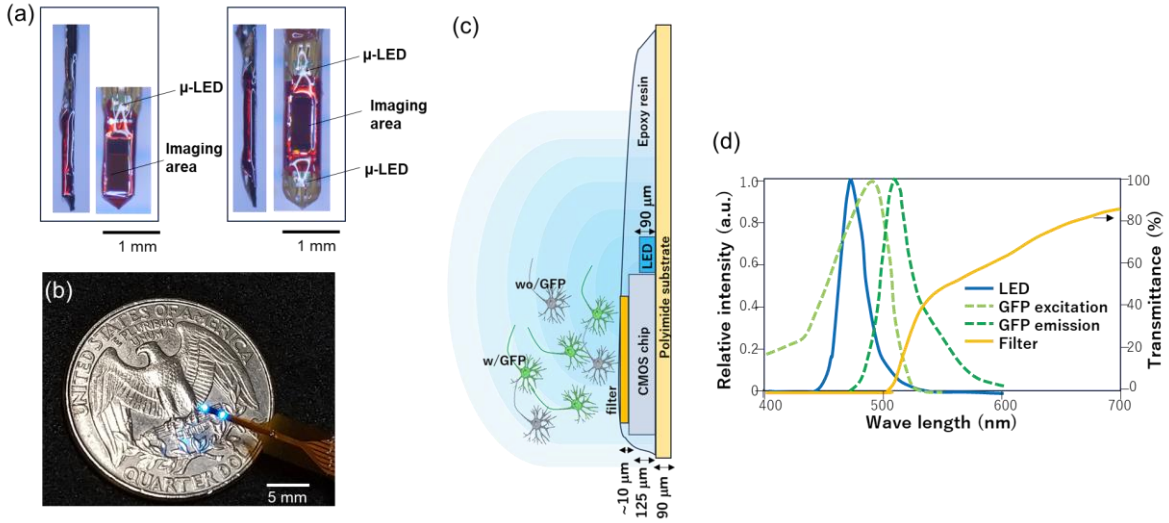

Figure 4. The structure of *i*-CIS device. **(a)** Photographs of two types of *i*-CIS devices with different numbers of μ-LEDs. The square on the left is equipped with one μ-LED, and the square on the right is equipped with two μ-LEDs. The left side is a side view, and the right side is a front view. An absorption filter is installed on the surface of the imaging area. **(b)** Photograph of an *i*-CIS device equipped with two μ-LEDs with the LEDs lit. Scale bar in **(a)** 1 mm, **(b)** 5 mm. **(c)** A schematic diagram of a cross-section of neurons expressing specific fluorescent proteins and an i-CIS device implanted in the brain. **(d)** Power spectra of blue μ-LED and the GFP excitation and emission, and the transmission characteristics of the absorption filter. Figure 4 **(a)** is modified from [10].

Figure 5(a) illustrates the *i*-CIS device implantation. The device, equipped with one or two µ-LEDs, raises concerns about heat generation when activated. To measure this, devices with two thermocouples were simultaneously implanted in two sites in anesthetized mice brains without cementing. The results are displayed in Figure 5(b-1), where the blue arrow indicates the LED activation and the green arrow indicates deactivation. The devices were implanted in the dorsal raphe nucleus (DRN) and amygdala (AMY). During the blue-light µ-LED activation at 0.5 mA, thermocouples were positioned near the LED and at the device tip, as marked by yellow circles in Figure 5(b-2). Upon activation of the LEDs, the temperature briefly rose by 0.2–0.3°C but quickly stabilized. After 1 hour, the temperature increase was only 0.4–0.7°C. About 5 minutes after turning off the LEDs, the temperature decreased by 0–0.2 °C. Given that a 2°C rise can influence neural activity [17,18], the temperature increase from the LEDs was deemed insignificant. The CMOS image sensor in the *i*-CIS device features a simple design without high-power components like operational amplifiers or analog–digital converters, resulting in low heat production. Additionally, the LED operates at around 0.5 mA, with the total power consumption of the *i*-CIS device being under 20 mW.

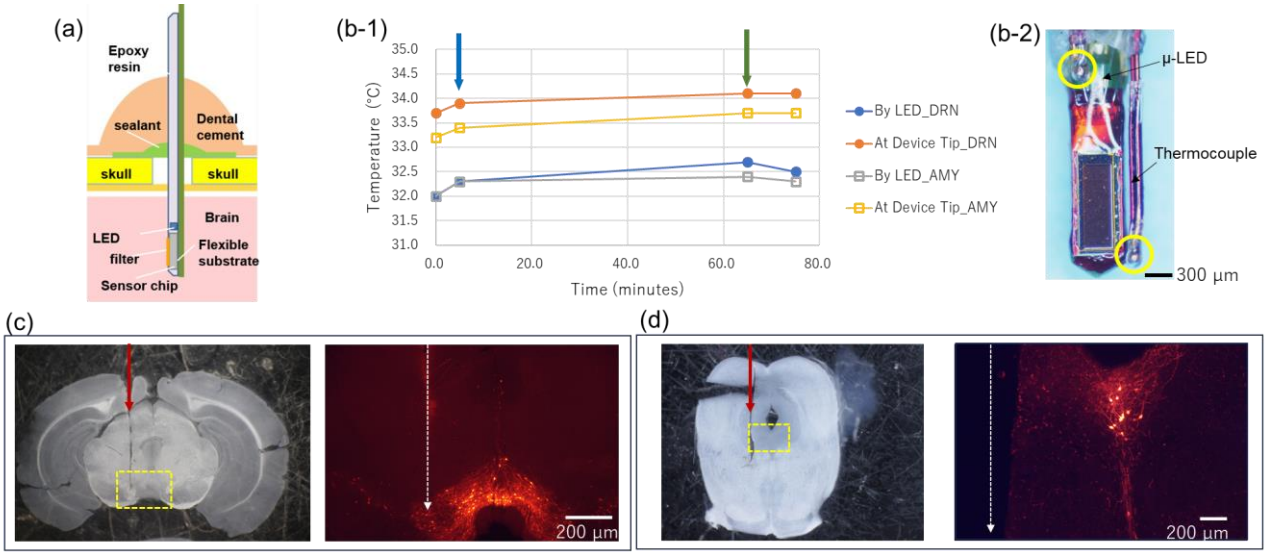

Figure 5. Device implantation. **(a)** Conceptual diagram of device implantation. **(b-1)** Results of temperature measurement after the device was implanted into the brain of a mouse and the mouse was anesthetized without being fixed with dental cement. The blue arrow indicates when the LED is on, and the green arrow indicates when the LED is off. **(b-2)** Photo of the thermocouples installed for temperature measurement and the *i*-CIS device. The yellow circles indicate the locations of the thermocouples. **(c)** Photo of a brain slice with the device implanted in the VTA and its fluorescence microscope image. The arrow indicates the device implantation position. The photo on the right is a fluorescence microscope image of the area enclosed by the dotted line in the photo on the left. **(d)** Photo of a brain slice with the device implanted in the DRN and its fluorescence microscope image. **(c)** and **(d)** Arrow indicates device implantation position. The photo on the right is a fluorescence microscope image of the area enclosed by the dotted line in the photo on the left. Scale bar: 300 µm in (b-2), 200 µm in **(c)** and **(d)**. Figure 5 **(b-1)** Caption [37].

The implantation position and fluorescent protein expression were confirmed post-imaging. Figure 5(c) shows coronal sections of a mouse brain injected with adeno-associated virus (AAV) into the ventral

tegmental area (VTA). The red arrow indicates the device insertion site. The device was embedded vertically, with the imaging area facing the brain's center. The fluorescence micrograph in Figure 5(c) confirms fluorescent protein expression in dopaminergic neurons using a red marker. The dotted arrow shows the implantation site, capturing dopamine cells. Figure 5(d) mirrors Figure 5(c) but with AAV injected into the DRN, marking serotonin neurons with a red fluorescent marker. In Figures 5(c) and (d), the yellow square in the left image is enlarged in the right fluorescence micrograph.

The imaging system included a control board, relay board, power supply, and systems for recording fluorescent images, along with a monitoring camera to capture and record mouse behavior simultaneously (Figure 6(a)). Figure 6(b) illustrates the experimental setup with freely moving mice. Calcium imaging data were obtained at approximately 10 frames per second (fps), and mouse behavior was monitored and recorded at ~30 fps using a video camera. Figure 6(c) presents a video of a freely moving mouse implanted with two *i*-CIS devices, showing concurrent changes in fluorescence intensity. The image at a specific time, such as during stimulation, can be used as the baseline (F_0), and the fluorescence difference image (ΔF) and fluorescence difference ratio image ($\Delta F/F_0$) from this baseline are calculated and displayed. Figure 6(d) depicts the algorithm for automatically extracting the region of interest (ROI) with the notable changes in fluorescence intensity [40].

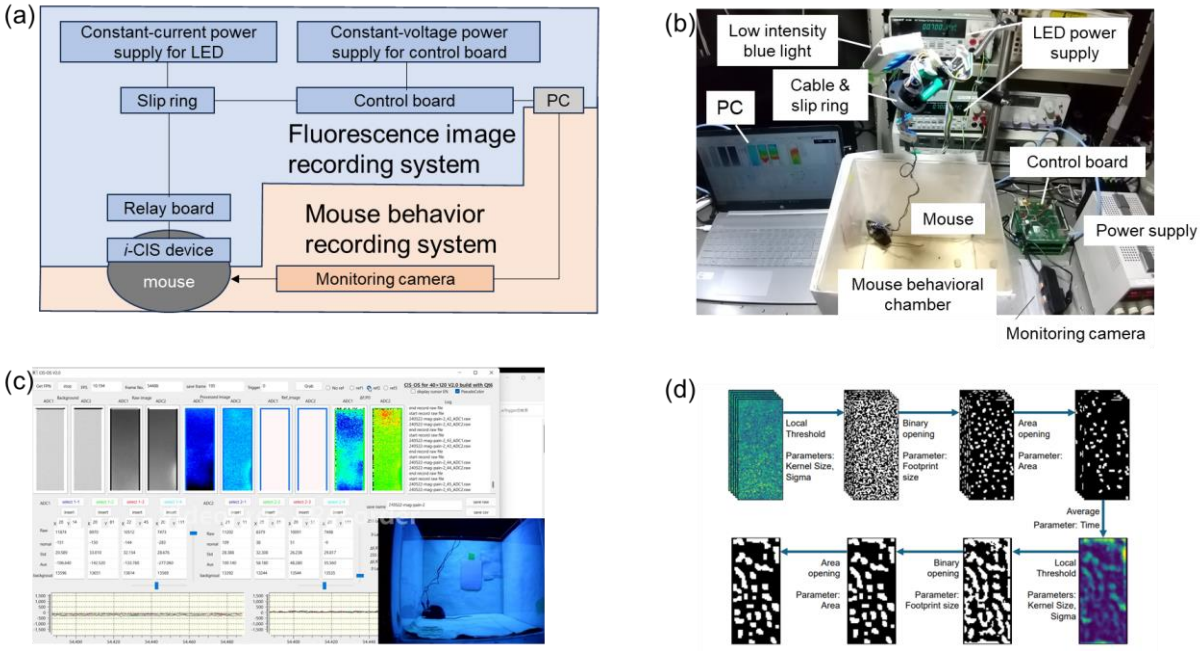

Figure 6. Fluorescence imaging system and analysis. **(a)** Conceptual diagram of fluorescence image recording system and mouse behavior recording system. **(b)**photo of the actual imaging system. **(c)** Photo of CIS_OS dual imaging GUI. This system can simultaneously record images from a monitoring camera observing mouse behavior. **(d)** Regions of interests (ROIs) algorithm overview. Schematic of ROI selection algorithm using color map (dark green for low values and bright yellow for high values). Figure 6 **(d)** Caption [40].

i-CIS devices lack a lens, preventing them from focusing on fluorescing neurons, making the image quality distance-dependent. The *i*-CIS mechanism for capturing *in vivo* fluorescent images has been analyzed based on fluorescence intensity and scattering relative to the device surface [39]. To ensure

that the regions selected from the image obtained by $\Delta F/F_0$ are not arbitrary, it is essential to localize and extract fluorescence intensity changes and separate the signal from the noise. An algorithm for ROI selection, involving adaptive binarizations with Gaussian and morphological image processing, was validated using both simulated and real data in free-moving conditions [40].

3.2. Examples of experimental results using the i-CIS device on freely moving mice

Here, we review four examples demonstrating the advantages of *i*-CIS devices.

(1) Dual implantation
(2) Imaging with another modality
(3) Measurement of neural activity in layered structures in the dorsoventral (DV) direction
(4) Integration with electrodes on a chip

3.2.1. Dual implantation

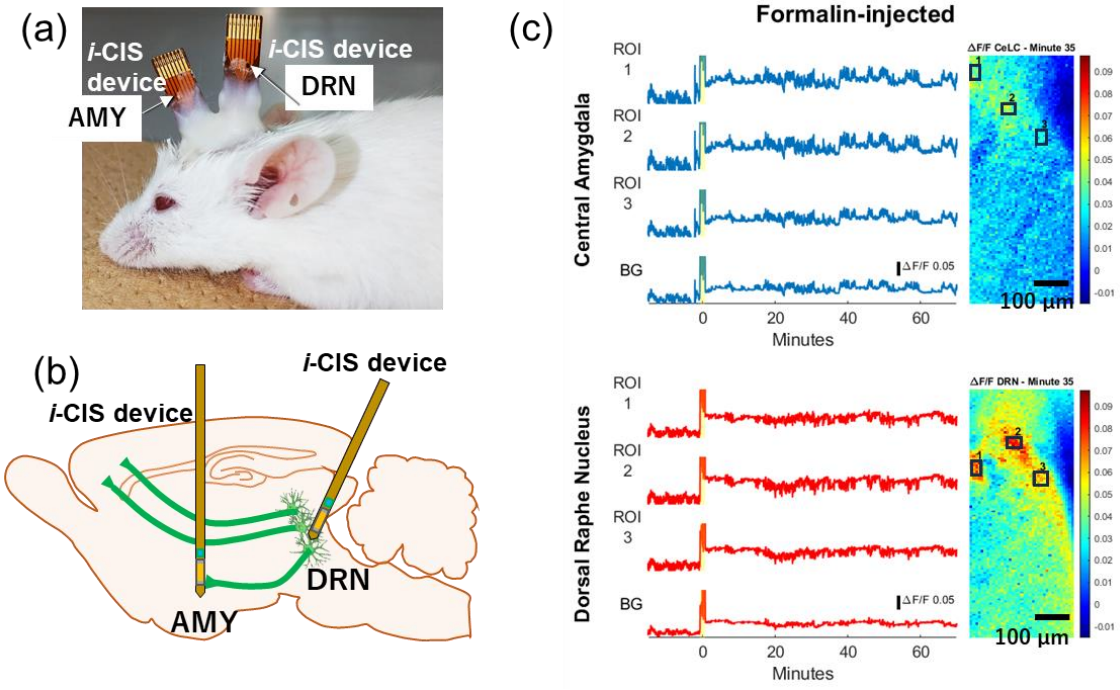

Figure 7. Dual implantation. **(a)**Photograph of a mouse with two *i*-CIS devices implanted in the DRN and AMY. Both *i*-CIS devices were implanted facing the midline, and in particular, in the DRN, the device was implanted at a 25° caudal angle to the vertical. **(b)** Schematic diagram of the mouse brain with the *i*-CIS devices implanted and serotonin neurons. **(c)** Calcium traces of specific ROIs. The graphs on the left show the time course of the change in fluorescence intensity (ΔF/F0) in each ROI of GCaMP6 in the DRN and AMY of mice that were injected with formalin to cause pain, and the images on the right show the fluorescence intensity (ΔF) of the imaging area. Figure 7 (c) Caption [12].

An example of observing neural activity during free movement is demonstrated by implanting the device at two locations simultaneously [37]. Pain is an immediate and powerful aversive event that activates associated brain regions with short latency; the neural network of pain-related signals is well-

documented [42–44]. Using G-CaMP6 mice, two locations were simultaneously imaged: the DRN, a nucleus in pain regulation housing serotonergic neurons [45], and the capsular-lateral central amygdala (CeLC), considered central to pain signal processing [46,47]. Serotonin neurons in the DRN partially project to the CeLC [48]. Both regions are involved in pain modulation [49] and are part of the system processing aversive stimuli and stress [50,51]. Figure 7(a) displays a mouse with the implanted device, while Figure 7(b) presents a conceptual diagram of the device. The device can be implanted in the DRN at a caudal angle of 25° taking into account the location of the ventricles and blood vessels, targeting the CeLC within the AMY. In this study, 2% Paraformaldehyde (PFA) was injected into the mice's hind paws to induce pain, with phosphate-buffered saline (PBS) as a control. Figure 7(c) shows representative fluorescence intensity changes and a time-lapse of these changes. Results indicated that pain stimulation increased neural activity in these regions.

The ROIs selected here were determined from the ΔF images and therefore were not automatically selected. This issue is resolved using the algorithm detailed in section 3.1.

3.2.2. Simultaneous imaging and another modality

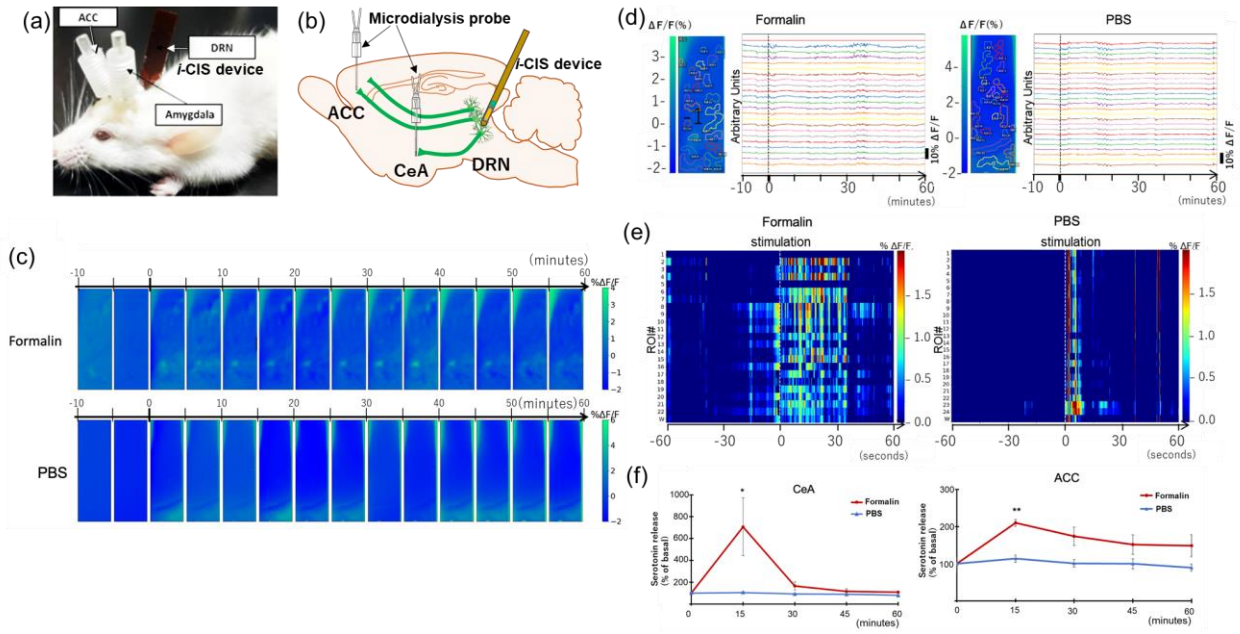

Figure 8. Simultaneous implantation of an imaging device with other modalities. **(a)** Photograph of a mouse implanted with the an *i*-CIS device and two microdialysis probes. **(b)** Schematic diagram of the mouse brain and serotonin neurons implanted with the *i*-CIS device and two microdialysis probes. **(c)** Representative examples of the average fluorescence changes every 5 min in the formalin and PBS groups. **(d)** Regions where fluorescence changes occurred were automatically extracted as ROIs using the analysis algorithm shown in Figure 3 (d) (left). Time lapse of the fluorescence intensity changes in each ROI (right). **(e)** Heat map of the fluorescence intensity changes over time in each ROI shown in **(d)**. **(f)** Changes in serotonin concentrations in the CeA and ACC measured every 15 min by microdialysis. All figures except Figure 8 **(b)** are taken from [11].

The advantages of the *i*-CIS device are its light weight and miniaturized, which allows other techniques such as microdialysis and electrophysiology to be used with the device. An *i*-CIS device was

implanted into the DRN of G-CaMP6 mice, and simultaneously microdialysis probes were implanted into the central nucleus of the amygdala (CeA) and anterior cingulate cortex (ACC) to measure serotonin release in response to pain stimuli [38]. Serotonin neurons in the DRN project to various brain regions, including the CeA and ACC. The CeA regulates emotions [55] and is crucial for pain [54], anxiety [55], and depression [56] as a center for nociceptive-specific information. The ACC is also a critical cortex area involved in pain processing and chronicity [57,58].

Figure 8(a) depicts a mouse with devices implanted in three regions, and Figure 8(b) presents a conceptual diagram. Figure 8(c) displays representative images of the average fluorescence change every 5 minutes in the formalin and PBS groups. Regions with large changes in fluorescence intensity were automatically selected by analysis using the algorithm detailed in section 3.1. This analysis addressed the issue of possible arbitrary ROI selection. Changes in fluorescence intensity over time for each ROI are shown in Figures 8(d) and 8(e). Neural activity was significantly higher in the formalin group compared to the normal group. Increased calcium fluorescence intensity during the acute and inflammatory phases indicates a biphasic pain response [59], confirming the biphasic pattern observed in the previous subsection. Figure 8(f) depicts serotonin concentration changes over time during microdialysis at the CeA and ACC projection sites. Microdialysis results did not show a biphasic effect. Samples were taken every 15 min, and images were acquired at approximately 10 fps, indicating potential differences in temporal resolution. The study measured left–right differences in pain stimulation, finding that contralateral stimulation increased DRN fluorescent activity. Microdialysis indicated that CeA serotonin concentration increased only after contralateral stimulation, while ACC serotonin release responded bilaterally. These significant results, obtained by simultaneous measurements in the same animal, are a benefit of the *i*-CIS device, as it allows simultaneous implantation of different modalities. Here, the analysis program described in Section 3.1 was used, so that non-arbitrary ROIs were automatically selected, overcoming the challenges in the previous subsection, 3.2.1.

3.2.3. Measurement of neural activity in layered structures in the DV direction

Because *i*-CIS devices are long in the direction of insertion, which is the dorsoventral (DV) direction, it is easy to observe the distribution of neural activity in the DV direction. This is advantageous because each area of the brain is often distributed in the DV direction. This is in contrast to passive devices such as GRIN lenses and image fibers, which observe the surface perpendicular to the direction of insertion. An example of the *i*-CIS device's advantages, specifically its ability to measure brain activity in the DV direction, is demonstrated by an imaging experiment in the hippocampus [21]. Temporal lobe epilepsy (TLE), the most common focal epilepsy [60, 61], is believed to originate from neural firing in the hippocampal dentate gyrus (DG). Research links the DG with other hippocampal areas and the CA1 and CA3 layered structures. Previous fiber photometry studies have noted regional hippocampal differences in TLE [62, 63]. This study, however, simultaneously observed the same event's layered structure in the same individual, capturing time and intensity differences in each layer, highlighting the i-CIS device's ability to simultaneously observe images in the DV direction.

An i-CIS device with two LEDs was implanted into the hippocampus of G-CaMP6 mice, a relatively shallow brain region. Figure 9(a) presents a conceptual diagram. Figures 9(b) and (c) illustrate a 40 × 120 pixel imaging area covering the hippocampus, divided into CA1, interlayer, and DG regions for

analysis. Imaging experiments were conducted for 1 h under freely moving conditions, followed by continuous recording post intraperitoneal kainic acid (KA) injection to induce epileptic symptoms.

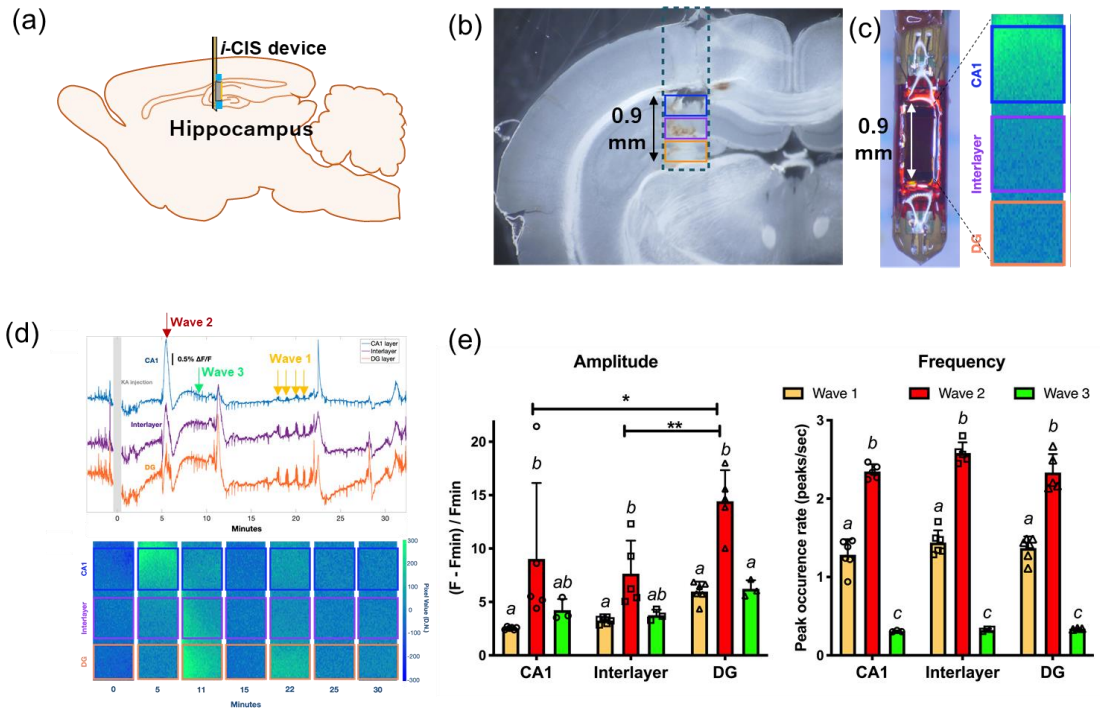

Figure 9. Measurement of neural activity in vertically oriented layers. **(a)**Schematic diagram of a mouse brain fitted with the *i*-CIS device. **(b)** Photograph of a mouse brain slice after the imaging experiment. The three boxed areas correspond to the layered structures of the hippocampus: CA1 (blue box), intermediate layer (purple box), and DG (orange box). The dotted box corresponds to the device implantation area. **(c)** Photograph of the *i*-CIS device and the three imaging areas corresponding to the three layers of the hippocampus**. (d)** Changes in fluorescence intensity over time in each of the three layers (top graph in **(d)**. Three characteristic waves of Waveform 1, Waveform 2, and Waveform 3, are shown. Images when characteristic changes in fluorescence intensity occurred (bottom image in **(d)**). (CA1, blue; intermediate layer, purple; DG, orange) (e) Peak calcium amplitude (left) and frequency (right) of the three waveforms in each layer. (Two-way ANOVA, *P < 0.05, **P < 0.005). (N = 6, 5, 3 for Wave 1, Wave 2, Wave 3). All figures except Figure 9 **(a)** are taken from [13].

Injecting KA is a recognized method for inducing seizures due to its excitotoxic properties [60,61]. The upper graph in Figure 9(d) displays the fluorescence intensity over time, revealing characteristic epileptic waveforms (wave1, wave2, and wave3). These waveforms match those from previous studies [62,63], confirming the *i*-CIS device's accuracy in recording neural signals. The images below illustrate changes in these waveforms.

Temporal differences in fluorescence intensity across the three regions were quantified by measuring amplitudes and frequencies, as shown in Figure 9(e), highlighting interlayer variations. Epileptic symptom stages were determined from the accompanying videos. Machine learning techniques, including long short-term memory and hidden Markov models, were utilized to classify seizure calcium activity and predict seizure behavior using multilayer image data.

Implanting the device in two locations simultaneously to observe CA3, CA1, and DG in the hippocampus can help identify temporal differences in amplitude and frequency, potentially leading to new findings valuable for future epileptic seizure treatments.

3.2.4. Integration of device and laser-carbonized electrode

Electrophysiological methods measure neural activity in the brain. Devices compatible with fluorescence imaging offer several benefits. We report on two integrated device types: one using a hybrid of separate FPCs [64], and another with an electrode fabricated by ball bonding integrated into the imaging device, with excitation light separately implanted [65]. In the new method introduced here, aluminum pads for electrodes are integrated at the CMOS chip design stage. An electrode is then fabricated by carbonizing the parylene film on the aluminum pad after waterproof and biocompatible parylene evaporation in the final fabrication process [66]. Figures 10(a) and 10(b) show a diagram and photograph of the device with integrated electrodes and a magnified photograph of the electrode. The laser-induced carbon electrode was characterized by cyclic voltammetry, electrochemical impedance spectroscopy, and X-ray photoelectron spectroscopy to confirm carbonization [66, 67].

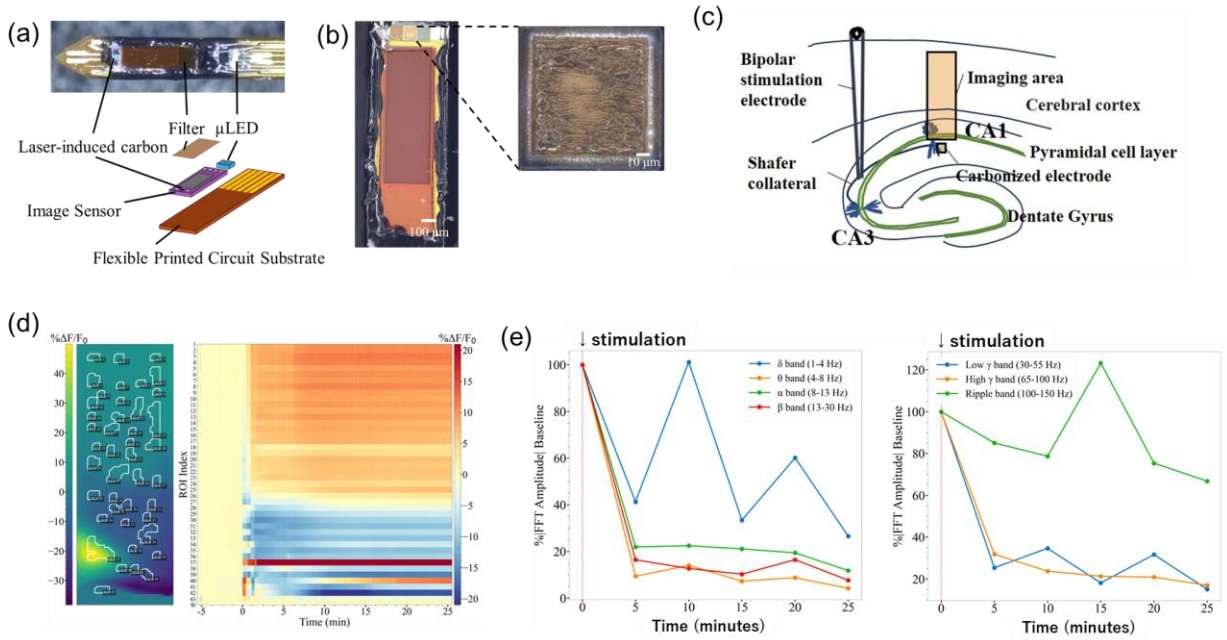

Figure 10. Integration of the *i*-CIS device with the laser carbonized electrode. **(a)** Schematic and photograph of the *i*-CIS device integrated with the laser carbonized electrode. **(b)** High magnification image of the *i*-CIS device imaging area and the laser carbonized electrode. **(c)** Schematic of the *i*-CIS device imaging area, the laser carbonized electrode, and the insertion location of the bipolar stimulating electrode. **(d)** Average image of fluorescence activity containing ROIs in the region from the hippocampus to the cerebral cortex (left) and a pseudo color time course of each ROI (right). **(e)** Results measured with a laser-carbonized electrode. Changes in FFT amplitude from baseline for δ, θ, α, and β (left graph), and low γ, high γ, and ripple bands in extracellular recordings (right graph). All figures caption [14].

The fabricated device was implanted into a mouse hippocampus, as illustrated in Figure 10(c). The bipolar electrode electrically stimulated the pyramidal cells in CA1, and neural activity was propagated to CA1 via Schaffer collaterals, and fluorescent imaging and extracellular potential measurements were performed in CA1. (Figures 10(d) and 10(e)). Fluorescence imaging results (Figure 10(d)) align with the hippocampus's layered structure and parts of the cerebral cortex (Figure 10(c)). Extracellular data analysis involved calculating the fast Fourier transform (FFT) amplitude change in various frequency bands from baseline levels, revealing a significant decrease post-stimulation in all bands except ripple and δ. This pattern mirrors the fluorescence signal progression in ROI 42 of the calcium imaging data. Increased activity in the ripple bands may correlate with heightened activity in ROI 37. These findings indicate that the implantable electrophysiological image-sensing device can concurrently record extracellular electrophysiological data and perform calcium imaging. Future research could explore the correlation between changes in extracellular potential and fluorescence intensity by adjusting electrode positions within the imaging area.

4. Implantable photostimulation device—PS device

This section reviews photostimulation devices based on LEDs described in Section 2.2.

4.1. Structure and features of PS device

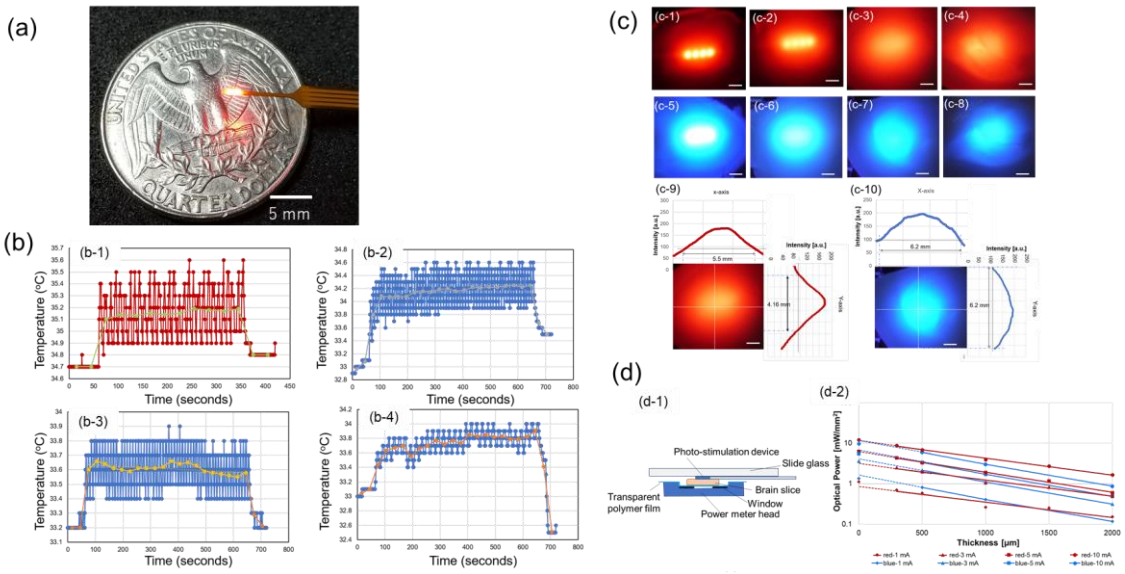

Figure 11. Characteristics of linear-type optical stimulation device. **(a)** The photos of the line type of PS device. scale bar: 5 mm **(b)** Graphs of the temperature measurement of the LED on the photo stimulation device implanted in the rat brain during operation. The numerical results and photo stimulation conditions are shown in Table 3. **(c)** Optical transmission measurements for PS device (line type) in rat brain slices. The photos of PS devices placed under rat brain slices in operation are shown in (c-1)-(c-8). The thickness of the rat brain slices is 300 μm for (c-1) and (c-5), 500 μm for (c-2) and (c-6), 1000 μm for (c-3) and (c-7), and 1500 μm for (c-4) and (c-8). All scale bars in (c) denote 1000 μm. The light intensity distribution is indicated in (c-9) and (c-10). (d) Optical power measurements for red or blue LEDs. **(d-1)** Schematic of the setup for measuring illumination power. A power meter receives light that passes through a thin rat brain slice**. (d-2)** Graph of light intensity change with different input currents and brain tissue thicknesses. All figures except Figure 9 **(a)** are taken from [19].

We first describe the characteristics of the LED used for photostimulation, including thermal and red and blue power transmittance measurements [30]. To activate ChR2 or ChrimsonR, nonselective cation channels used in optogenetics, the PS device contained blue (470 nm) or red LEDs (620 nm). In general, the minimal light power density required to activate ChR2 and ChrimsonR is defined as P_{stim}, which is 1 mW/mm^2 [68]. Unlike the prolonged imaging described in Section 3.1, optical stimuli involved short-duration light exposure. However, since the PS device is implanted in or on the brain and uses a high-power LED, the heat generated to achieve this intensity density was a concern, confirmed in this study. Figure 11(a) illustrates the linear PS device for ChrimsonR, while Figure 11(b) presents the temperature characteristics measured under the experimental light stimulation conditions. Rat experiments involved 5 minutes of red LED stimulation for ChrimsonR (Figure 11(b-1)), and monkey experiments involved 10 minutes of blue LED stimulation for ChR2 (Figure 11(b-2, 3, 4)), so the temperature measurements were performed under the same conditions. Measurements were performed by placing thermocouples on the PS device LEDs and inserting them onto the rat brain surface. Table 2 details the measurement conditions and resulting temperature increases. Rats were anesthetized without dental cement fixation. Under the most extreme conditions (Figure 11(b-4)), the maximum temperature rise was less than 2°C. Given that temperature increases would be mitigated by cerebrospinal fluid and blood flow when fixed with cement or in freely moving rats, these findings suggest minimal impact of the PS device on neurons under the specified photostimulation conditions.

Table 2. Temperature measurement and photo stimulation conditions.

	LED	Type	Current (mA)	Frequency (Hz)	Duty (%)	Time (minutes)	Temperature up (°C) average
(b-1)	red	linear	3.0	2.0	20.0	5.0	0.40
(b-2)	blue	planar	2.0	2.0	40.0	10.0	0.89
(b-3)	blue	linear	3.0	2.0	20.0	10.0	0.36
(b-4)	blue	linear	3.0	1.0	40.0	10.0	0.61

Light transmission in rat brains was examined using ChrimsonR and ChR2 PS devices. Fixed rat brain sections (300, 500, 1000, and 1500 μm) were placed on a linear-type PS device, and images of the sections were taken, as shown in Figure 11(c). Figures 11(c-9) and 11(c-10) present graphs of the light spread from the PS device for ChrimsonR and ChR2. Figure 11(d-1) depicts the setup schematic for measuring illumination power relative to the thickness of the brain slices on each PS device, with results shown in Figure 11(d-2). The red LED penetrated deeper than the blue LED, consistent with prior findings that brain tissue absorption is similar for both wavelengths, but scattering affects blue light more [69,70]. LED injection currents above 3 mA were sufficient to activate ChR2 channels in the rat brain at a 1 mm depth. In monkey experiments, activating ChR2 in the prefrontal cortex (PFC) was necessary. Histology indicated ChR2 expression at less than 0.5 mm below the PFC surface [17,18], demonstrating that a 2-mA injection current suffices to stimulate ChR2 in the monkey PFC.

4.2. Example of experimental results using the PS device on freely moving mice

Similar to Section 3.2, herein, we examine previous studies showcasing the benefits of PS devices, including the ability to directly irradiate arbitrary and deep areas with design flexibility. Utilizing this flexibility, we will look at two types of PS devices: linear and ring, tailored for area-specific photostimulation. For monkeys, a device was developed for region-selective photostimulation over a large area. To study the activation of light-activated proteins, a microdialysis device was implanted at the projection site of the light-stimulated neurons to measure neurotransmitter concentrations.

4.2.1. PS device for rodents

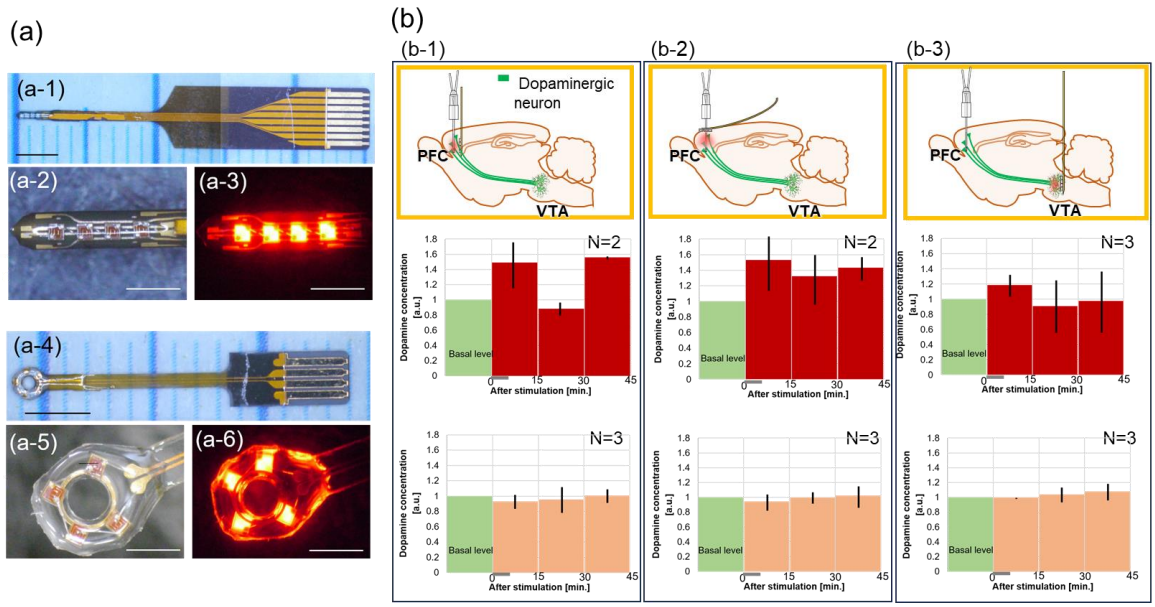

Figure 12. Photo-stimulation device for rodent. **(a)** Photos of the PS device for rodents. The photos of the line type of PS device show in **(a-1)-(a-3)**. The photos of the ring type of PS device show in **(a-4)-(a-6)**. Scale bar: 3 mm in **(a-1)** and **(a-4)**, 1 mm in **(a-2)**, **(a-3)**, **(a-5)**, and **(a-6)**. **(b)** Measurement of dopamine concentration changes using microdialysis with a PS device. The top diagrams show the schematic diagrams of the implantation position of the PS device and microdialysis probe in the rat brain, the middle diagrams show the results in a rat brain expressing ChrimsonR, and the bottom diagrams show the results in a wild-type rat brain not expressing ChrimsonR. **(b-1)** The line-type PS device was implanted in the PFC, and the microdialysis probe was also implanted in the PFC. **(b-2)** A ring-type PS device was placed on the brain surface, and the microdialysis probe was passed through a hole in the ring and implanted in the PFC. **(b-3)** The line-type PS device was implanted in the VTA, and the microdialysis probe in the PFC. The gray horizontal line in the graph indicates the PS time period, 5 minutes. The number of trials; N is shown in each graph. Error bars indicate standard deviations All figures are taken from [30].

Two types of PS devices, linear and ring, were fabricated for rodents. To evaluate the PS device, the light-sensitive protein ChrimsonR was expressed in the rat VTA of the mesolimbic dopaminergic system, and a PS device with red LEDs and a microdialysis probe was implanted in the PFC to measure dopamine levels [30]. AAV-DJ-Syn-ChrimsonR-tdTomato was injected into the VTA of rats, PS devices were implanted in the VTA or PFC, and microdialysis probes were implanted in the PFC. Control experiments were carried out in the same way without AAV injection. AAV expression was

confirmed using tdTomato as a marker. Figure 12(a-1), (a-2), and (a-3) illustrate thin, needle-like linear PS devices that are easy to insert and minimally invasive to brain tissue. Figure 12(a-4), (a-5), and (a-6) depict ring-type PS devices, which allow for the insertion of a microdialysis probe into the central hole to measure neurotransmitter levels in the PFC below the cortex using light stimulation, benefiting from micro-LEDs. Figure 12(b) details the PS device and microdialysis probe placement, a schematic of dopamine neurons, and measurement results in rats with and without ChrimsonR expression, under the photostimulation conditions listed in Table 2 (b-1). All microdialysis probes were implanted in the PFC, but the PS device types and implantation sites varied: linear-type PS device/PFC (Figure 12(b-1)), ring-type PS device/PFC (Figure 12(b-2)), and linear-type PS device/VTA (Figure 12(b-3)). Dopamine levels remained unchanged in control rats post-photostimulation. However, in ChrimsonR-expressing rats, dopamine levels in the PFC rose immediately after stimulation, indicating the PS device's efficacy for photostimulation.

4.2.2. PS device for monkeys

AAV-DJ-CAG-ChR2(H134R)-tdTomato was injected into the monkey VTA. Two types of PS devices were created: a linear type with three LEDs and a planar type with 6 × 8 LEDs for dopamine measurement via microdialysis [30]. Photographs of these devices are shown in Figures 13(a) and 13(b). The planar PS device, featuring 6 × 8 LEDs, allows six vertical LEDs in Figure 13(b) to be lit simultaneously and eight rows to be selectively activated. μ-LEDs offer the advantage of stimulating a large 9 × 6.5 mm^2 area and provide design flexibility. To measure neurotransmitter levels in the PFC beneath the cortical surface, a PS device with nine holes for microdialysis probes was designed. The positions of the PS device and microdialysis probe, a schematic of dopamine neurons, and the measurement results are depicted in Figures 13(c) and 13(d). The photo stimulation conditions were the same as those in (b-4) and (b-2) of Table 2, respectively. Microdialysis collection and measurements were the same as those in the rodent model, with probes implanted in the PFC. However, the PS device type and implantation position varied. As Figure 13(c-1) illustrates, a linear-type PS device was implanted in the VTA, located using MRI and CT [68]. Under weak conditions (P_{stim} < 1 mW/mm^2) with a 1 mA LED current, dopamine concentration remained unchanged post-photostimulation, consistent with Section 4.1 results (Figure 13(c-2)). Conversely, under pulse conditions with a 3 mA LED current and 20% and 40% duty ratios (P_{stim} > 1 mW/mm^2), dopamine concentration increased post-photostimulation (Figure 13(c-3)). Figure 13(d-1) depicts the experimental setup with a planar PS device and microdialysis probe in the PFC. Figure 13(d-2) shows the position of each hole in the PS device. Dopamine concentration measurements using holes 3 and 8 are presented in Figures 13(d-3) and (d-4), respectively, with dopamine dialysates collected simultaneously from both holes.

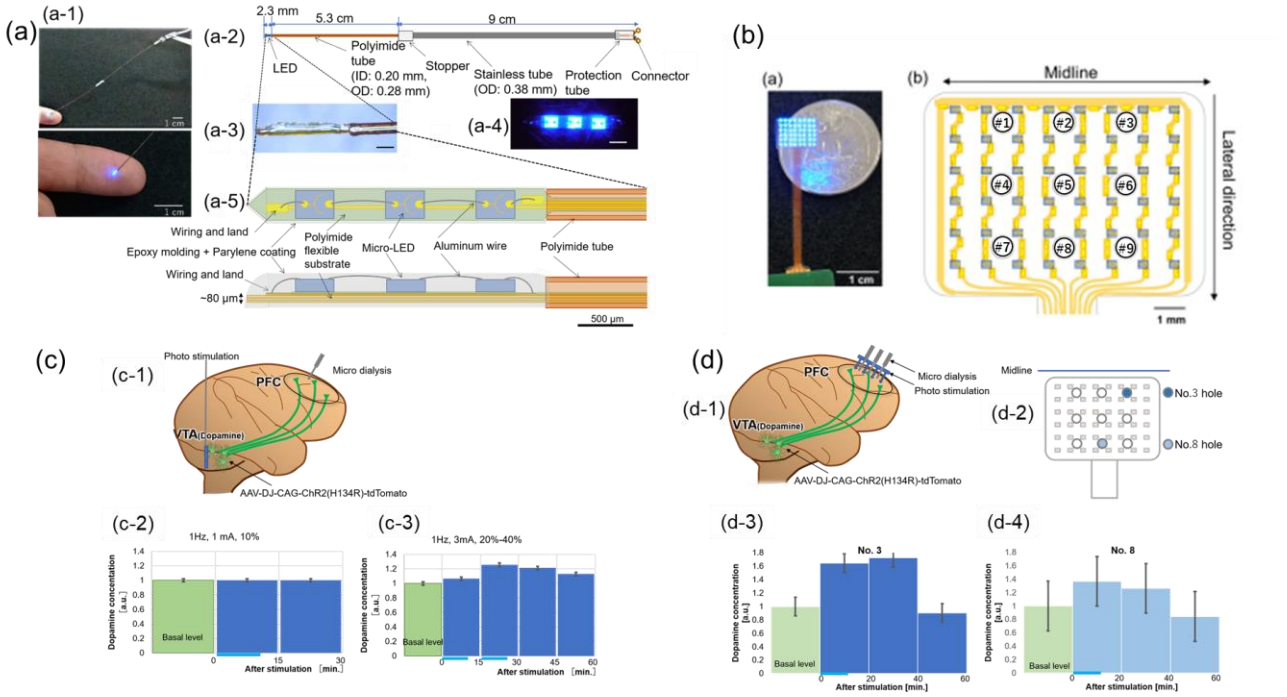

Figure 13. Photo-stimulation device for monkeys. **(a)** Photographs of the line-type PS device for monkeys and explanatory diagrams of its structure. The photos of the line-type of PS device show in **(a-1)**, **(a-3)**, and **(a-4)**. The structure of the line-type PS device is shown in **(a-2)** and **(a-5)**. Scale bar: 1 cm in (**a-1**), 500 µm in (**a-3**, **a-4**, and **a-5**). **(b)** Photograph of the planar-type PS device for monkeys and an explanatory diagram of its structure. #1 to #9 in the figure are holes for inserting microdialysis probes. Scale bar: 1 cm in **(b-1)**, 1 mm in **(b-2)**. **(c)** Measurement of dopamine concentrations using a line-type PS device implanted in the VTA and microdialysis in the PFC. A schematic diagram is shown in **(c-1)**. The results of dopamine concentration are shown in **(c-2)** and **(c-3)**. **(d)** A planar-type PS device was placed on the brain surface, and the microdialysis probe was passed through a hole of the PS device and implanted in the PFC. A schematic diagram is shown in **(d-1)**. The positions of each hole are indicated in **(d-2)**. The results of measuring dopamine concentration using different positions of the holes for inserting the microdialysis probe are shown in **(d-3)** and **(d-4)**, respectively. The light blue horizontal line in the graph indicates the PS time period, 10 minutes. All figures are taken from [30].

4.3. Evaluation of PS devices in studies of optogenetics

Optogenetics, utilizing light-sensitive proteins and genetic engineering, has significantly advanced the understanding of neural connections and functions by activating or inhibiting specific neurons, and has facilitated behavioral studies in animals, including primates. Despite numerous reports on behavioral changes due to optogenetic light stimulation, few have detailed the measurement of neurotransmitter release or its properties following photostimulation. This report provides scientifically verified findings using photostimulation devices. Moreover, the results corroborate previous studies that used photostimulation with electrophysiology or fast-scan cyclic voltammetry to investigate dopaminergic neuron projections via ChR2 expression in rodents [72,73].

5. Photoceutical devices—optical diagnostic and therapeutic devices

Section 3 discusses implantable fluorescent imaging devices that monitor neuronal activity by imaging changes in the fluorescence intensity of the GCaMP6 protein in neurons. Section 4 reviews implantable photostimulation devices that modify neuronal activity using LED lights. From a medical standpoint, measuring neural activity through fluorescence imaging can aid in disease diagnosis, while photostimulation to control neural activity can be utilized for treatment purposes. This approach paves the way for a system that integrates both diagnosis and therapy using implantable optoelectronic devices, referred to as "photoceuticals." Next, we will discuss photoceuticals.

Figure 14 compares photoceuticals with pharmaceuticals and electroceuticals. Pharmaceuticals, which use medicines, can have specific effects but also cause systemic side effects. Electroceutical devices, currently under research [74], treat affected areas locally, potentially reducing side effects. Combining these devices with measurement tools allows for closed-loop processing, which may lead to early diagnosis and effective treatment. An example is an epileptic seizure treatment device [75], where an ECoG device on the brain surface detects seizure signs, and electrodes in the brain electrically stimulate to suppress seizures. However, electrical measurement and stimulation lack specificity. For instance, electrophysiological measurements struggle to identify if targeted cells are activated, and electrical stimulation affects all cells around the electrode, potentially causing side effects.

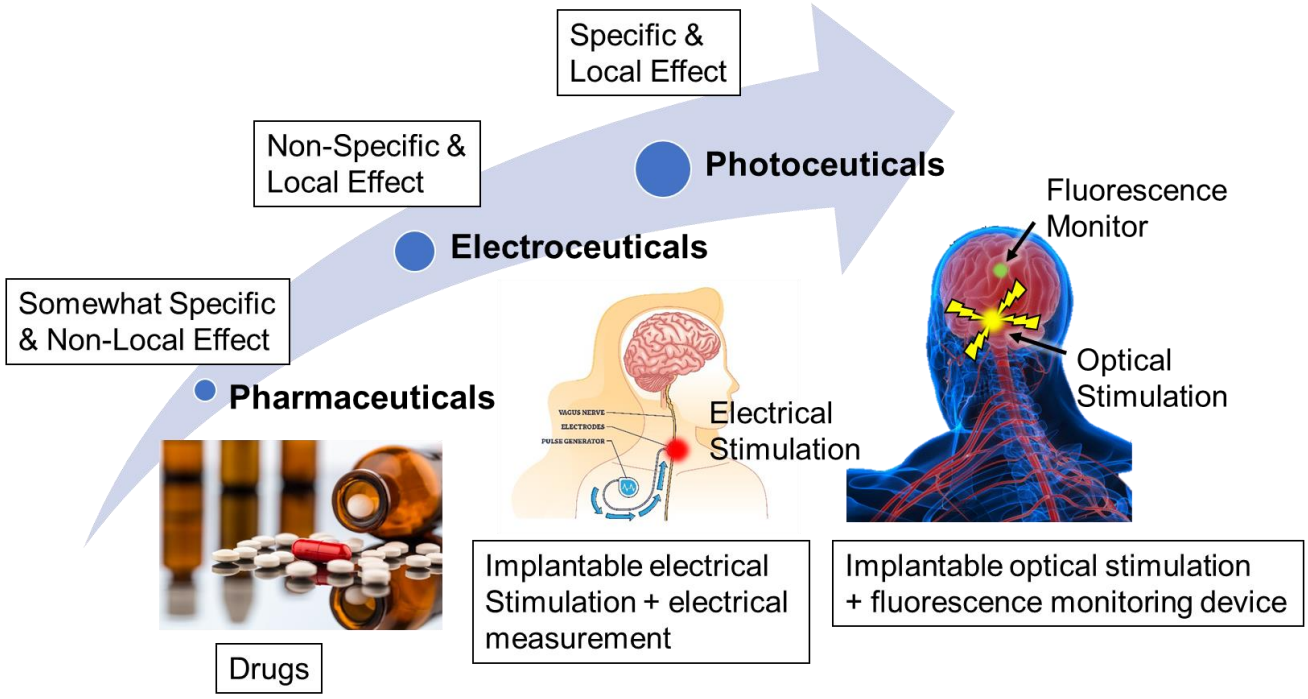

Figure 14. Concept of Photoceuticals compared to Pharmacetuticals and Electrocetuticals [12].

Genetic engineering enables precise light-based measurements and stimulations, allowing ultrasmall implanted optoelectronic devices to facilitate early diagnosis and treatment, termed photoceutical devices [12]. Implantable CMOS imaging devices and LED light stimulation devices, which support free movement, have potential applications as photoceuticals. The next section discusses the development efforts for these devices.

5.1. Example of experimental results as the beginning of photoceutical system

To date, fluorescence imaging using optogenetics as alternatives to traditional electrophysiology have been explored. In the search for a photo-pharmacological system, we discuss several examples: observing postsynaptic receptors in a pharmacologically effective neural circuit, combining optogenetics with immunostaining for pharmacological elucidation, integrating ECoG with a photostimulator to demonstrate human application in primates, and combining a PS device with an *i*-CIS device for simultaneous observation and treatment. Additionally, we present research on integrating brain–machine interfaces (BMIs) with photostimulation and capturing entire neural circuits, highlighting the potential of the photoceutical system for simultaneous observation and treatment in humans.

5.1.1. Fluorescence imaging using an *i*-CIS device in the nucleus accumbens of mice expressing dLight1.2 upon drug administration

In the mesolimbic reward system, dopamine neuron activity from the VTA to the nucleus accumbens (NAc) is crucial for regulating memory, emotions, motivation, behavior, and addiction [76,77]. Imaging devices help visualize how different drugs affect dopamine release, aiding addiction treatment. Recently, diverse AAVs and neurotransmitter receptor-side biosensors have become prevalent. dLight1.2, a fluorescent protein, increases in intensity when dopamine binds to its receptor [78]. Using the *i*-CIS device, the release of dopamine can be visualized in real-time by tracking dLight1.2 fluorescence changes in the NAc, measuring dopaminergic neuron activity from the VTA to NAc [79].

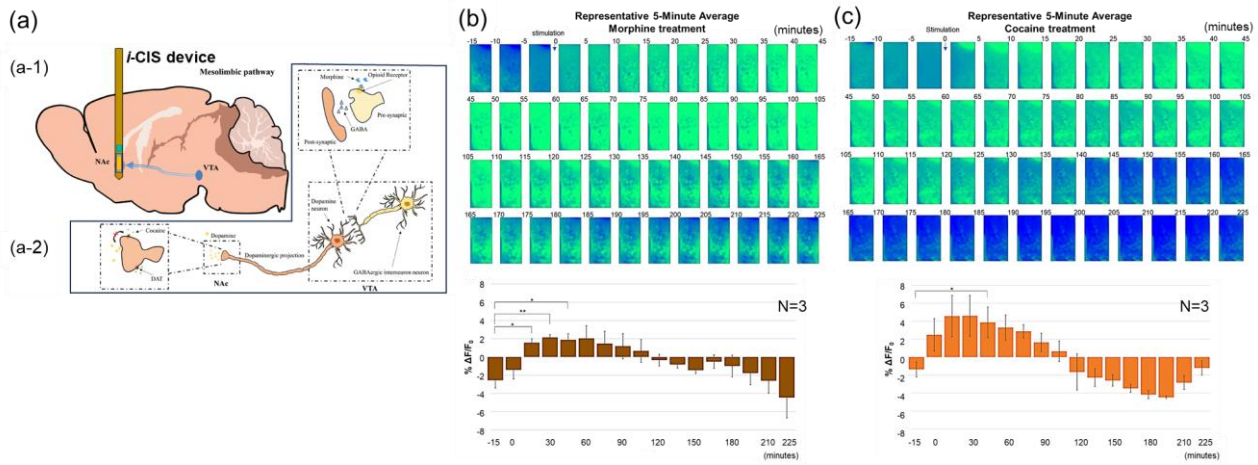

Figure 15. Fluorescence imaging using an *i*-CIS device in the NAc of mice expressing the dLight1.2 upon drug administration. **(a)** Schematic diagram of the mouse brain with an *i*-CIS device is indicated in **(a-1)** and schematic diagrams of the relationship between dopamine neurons and GABAergic neurons in the mesolimbic pathway upon drug administration in **(a-2)**. **(b)** The time course of the averaged image every 5 minutes (top) and the numerical graph (bottom) of the image in the NAc upon morphine administration. **(c)** The time course of the averaged image every 5 minutes (top) and the numerical graph (bottom) of the image in the NAc upon cocaine administration. All figures are taken from [79].

Figure 15(a-1) depicts the mesolimbic pathway and the *i*-CIS device implanted in the NAc. Figure 15(a-2) illustrates the connections between dopaminergic and GABAergic neurons and their interaction with drug action. Figures 15(b) and (c) display changes in fluorescence intensity in the NAc following morphine and cocaine administration, respectively. While both drugs target dopaminergic neurons, morphine inhibits opioid receptors at presynaptic terminals [80], and cocaine obstructs dopamine transporter (DAT) proteins [81]. A 4-h imaging experiment demonstrated the differing kinetics of dopamine release in the NAc induced by these drugs, enabled by *i*-CIS devices' benefits in pharmacological studies. The *i*-CIS device, being lightweight and compact, along with its lightweight relay board and cables, permits extended observation of mice without causing stress. Additionally, intraperitoneal injection or oral administration can be easily conducted during imaging, making the *i*-CIS device ideal for studying pharmacological dynamics.

5.1.2. Evaluation of drug effects using a photostimulation and microdialysis system

We described the evaluation of photostimulation devices in anesthetized rats and the measurement of neurotransmitter concentrations during microdialysis in Section 4.2.1. Here, we present an optogenetic experiment under free-moving conditions using mice expressing ChrimsonR in the VTA [82].

Figures 16(a)-(d) illustrate an overview of dopaminergic neurons in the mouse VTA with a PS device and NAc with a microdialysis probe, a photograph of the mouse during the experiment (notably during light stimulation), the relationship with GABAergic neurons, and a section of the perfusion-fixed brain post-experiment showing the implantation site. Transgenic mice expressing DAT-dependent Cre were used to study GABAergic neurons' involvement in dopamine neurons. EF1a-DIO-Chrimson-R-mRuby2-KV2.1 was injected into the VTA of DAT-cre mice to express ChrimsonR specifically in dopaminergic neurons, while CamKIIa-ChrimsonR-mScarlet-KV2.1 was injected into the VTA of wild-type mice to express ChrimsonR non-specifically. Figure 16(e) shows the change in dopamine concentration in the NAc before and after photostimulation for three different cases. Figure 16(e-1) presents results from mice with ChrimsonR expressed specifically in dopamine neurons. Figure 16(e-2) displays results from mice with ChrimsonR expressed non-specifically in dopamine neurons. Figure 16(e-3) shows results from mice with non-specific ChrimsonR expression in dopamine neurons intraperitoneally injected with bicuculline, a $GABA_A$ receptor antagonist [83]. Microdialysis indicated that photostimulation in the VTA specifically targeting dopamine neurons increased dopamine concentration. In contrast, non-specific photostimulation did not increase dopamine concentration. However, non-specific photostimulation combined with $GABA_A$ receptor suppression via bicuculline increased dopamine concentration. These findings, supported by immunostaining (details in [82]), elucidate the interaction between GABAergic and dopamine neurons (Figure 16(a)).

The PS device and system proved effective in pharmacological experiments, enabling intraperitoneal drug injection without stressing the mouse during imaging, thus allowing proper observation of drug efficacy. Optimal conditions for light stimulation, such as frequency, duration, and rest intervals, remain to be fully determined. Additionally, to prevent synaptic vesicle depletion, more effective conditions are needed. However, in optogenetic experiments, pulsed photostimulation mitigates the issue of temperature rise.

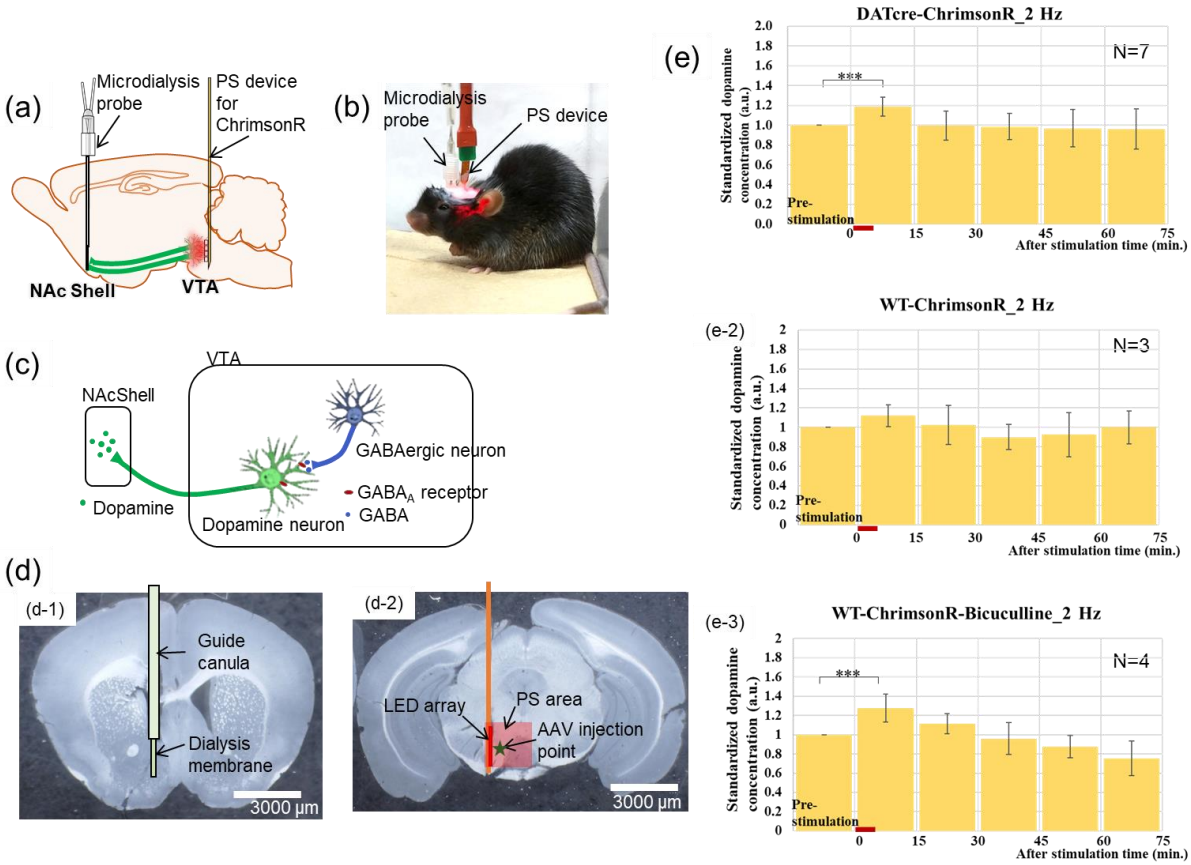

Figure 16. Evaluation of drug effects using a photo-stimulation and microdialysis system. **(a)** Schematic diagram of the mouse brain with a device and a microdialysis probe implanted and dopamine neurons. **(b)** Photograph of a mouse undergoing photo-stimulation under free-living conditions. **(c)** schematic diagram of the relationship between dopamine neuron with GABA receptors and GABAergic neuron in the mesolimbic pathway. **(d)** Photographs of mouse brain slice. **(d-1)** Photomicrograph of a coronal slice of mouse brain at NAc, showing the position of the microdialysis probe superimposed**. (d-2)** Coronal slice of mouse brain at VTA, showing the position of PS device implantation, LED array area (red line in the figure), LED irradiation area (light red square in the figure), and AAV injection position (green star in the figure). Scale bars: 3000 μm **(d-1)**, **(d-2)**. **(e)** In the order of **(e-1)** to **(e-3)**, mice expressing ChrimsonR specifically in the VTA of dopaminergic neurons, wild-type mice expressing ChrimsonR non-specifically in the VTA of dopaminergic neurons, and wild-type mice expressing ChrimsonR in the VTA that were injected intraperitoneally with bicuculline were used. The red line in the graph indicates the 5-minute period during which photo-stimulation was performed. All figures are taken from [31].

5.1.3. Combined LED/ECoG array device for monkeys

BMI technology is under development [84–86], connecting the brain to machines. This review discusses an integrated PS device and ECoG for electroencephalography as a BMI method [35]. Macaque monkeys with bilateral VTA regions injected with AAV2.1-Syn-ChrimsonR-tdTomato were trained in a high-risk, high-return versus low-risk, low-return task [87]. The mesofrontal dopaminergic pathway from the

VTA to ventral Brodmann area 6 (6V) is crucial for risk-related decision-making [88]. Two LED/ECoG array devices were implanted into the 6V region of the monkey brain on both sides.

Figure 17(a) displays the combined LED/ECoG array device used in this study. The device, with its 18 electrodes and 29 LEDs, was designed to fit the 6V region, maintaining symmetrical construction for both brain hemispheres. The LED and ECoG electrode pitches were 2.5 mm. The LEDs had a center emission wavelength of 625 nm and a size of 500 μm × 500 μm. The Pt ECoG electrodes had a convex diameter of 0.8 mm and an overall diameter of 2.1 mm. LEDs were controlled via X-Y addressing, while ECoG electrodes were wired independently with ground and reference electrodes on opposite sides. The LED and ECoG substrates were made of transparent polyimide and urethane, respectively. Owing to the one-piece design, epoxy resin pillars were used to secure the LEDs to the ECoG probe, also aiding in LED light guidance. The electrode shape was molded to follow the cortical surface. Figure 17(b) shows the device with all LEDs lit mounted on a monkey brain model.

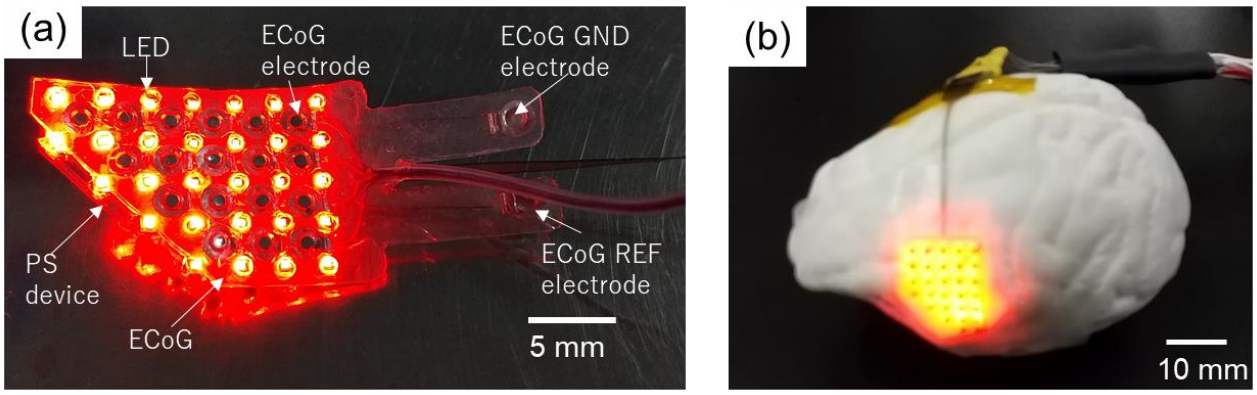

Figure 17. The combined LED/ECoG array device. **(a)** A photograph of the stacked device with a 29-LED array and an 18-ECoG electrode array. Scale bar: 5 mm. **(b)** A photograph of the placement of the fabricated device on a monkey brain model. Scale bar: 10 mm.

Region-specific photostimulation within the 6V modulated risk-dependent decision-making process highlighted the distinct roles of its subregions. Activation of the VTA 6V pathway led to cumulative modulatory effects, suggesting long-term dopamine-dependent plasticity mechanisms altered neural responses. The successful long-term implantation of the combined LED/ECoG array device demonstrated its effectiveness for chronic observations. This primate study is significant for understanding the neural mechanisms of human gambling disorders. Additionally, the device's optogenetic technology and BMI applicability extend to both rodents and primates. In addition to the physiological implications of these findings, it is noteworthy that optogenetic technology and the combined elements of the device and BMI can be used in both rodents and primates.

5.1.4. Photostimulation by the PS device and fluorescence imaging measurement system

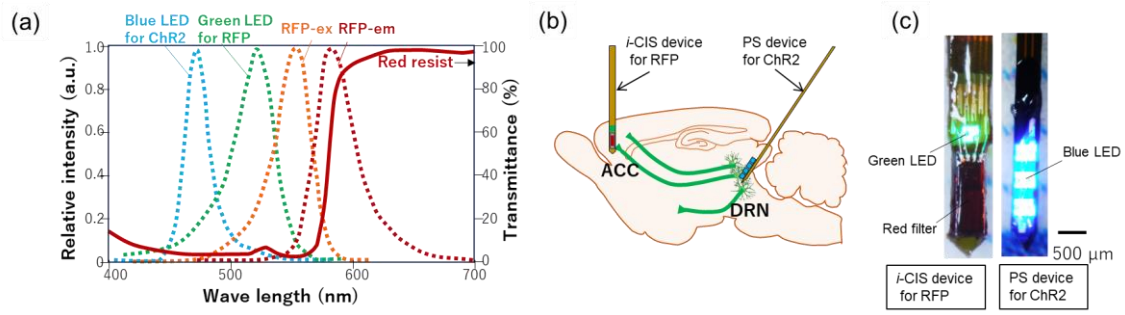

Figure 18. Photo-stimulation by PS device and fluorescence imaging measurement system. **(a)** Power spectra of blue μ-LED for ChR2, green μ-LED for RFP, the RFP excitation and emission, and the transmission characteristics of the absorption filter. **(b)** Schematic diagram of the mouse brain with a PS device and an *i*-CIS device for RFP, and serotonin neurons. **(c)** Photographs of an *i*-CIS device for RFP (left) and a PS device for ChR2 (right). Scale bar: 500 μm.

We reviewed the *i*-CIS device and the combination of PS with other modalities. This study illustrates the use of light for imaging and stimulation to create photoceuticals. Light with a wavelength of 620 nm, which activates Chrimson R, is transmitted through the GFP sensor's absorption filter. Conversely, optogenetics typically uses such high light intensity that even 470-nm light, which activates ChR2, can penetrate the GFP sensor's absorption filter. Figure 18(a) demonstrates that an effective pairing includes an imaging device with a red absorption filter for red fluorescent proteins (RFP), like RGECO [89] or the red GRAB sensor [90], and a PS device for ChR2. Figure 18(b) illustrates a mouse brain schematic with a blue PS device and an *i*-CIS device for RFP implanted in the serotonin neuron system. The blue PS device is implanted in the DRN expressing ChR2, and the *i*-CIS device for RFP is implanted in the ACC expressing RFP. Figure 18(c) shows the RFP device with a red absorption filter and green LED for RFP activation, alongside the blue PS device. RFP devices have been confirmed as effective imaging sensors. The PS device's LED periphery was shielded with black resist to limit lateral light diffusion, though some light still transmitted through the *i*-CIS device's red filter for RFP. The above results suggest that the combination of photostimulation and fluorescence imaging shows potential for future development in diagnosis and treatment with light.

5.2. Current status and photoceutical prospects for observation and treatment

This section reviews recent studies on neural circuits and closed-loop systems, which are crucial for photoceutical devices and include optical diagnostic and therapeutic tools. Elucidating neural networks has been proposed for pain treatment, with reports on pain regulation in the DRN-VTA-NAc pathway and the ACC-VTA-ACC positive feedback circuit in neuropathic pain [91,92]. Additionally, the mid-cingulate cortex-posterior insula pathway, along with the ACC, is implicated in promoting pain sensation and the transition from acute to chronic pain [93]. There have also been reports of combining BMIs and optogenetics to treat pain by adapting it to a closed-loop system including the primary somatosensory cortex and the ACC [94,95]. Beyond pain, there are clinical applications for TLE, such as suppressing

intrahippocampal seizures through electrical stimulation of the medial septum (MS) in the closed MS-hippocampal loop [96–98].

6. Conclusion

This review discusses current research on small implantable optoelectronic devices for measuring and stimulating small animals, like mice, while allowing free movement. It outlines the structure and characteristics of the *i*-CIS and PS devices and provides usage examples. *i*-CIS and PS devices are compact and lightweight, allowing multiple implants in mice without stress. These systems facilitate simultaneous long-term fluorescence imaging, optical stimulation, and behavioral observation, benefiting neuroscience and pharmacology. These devices hold potential for photoceutical applications. The use of *i*-CIS and PS devices in primates may broaden their future applications to humans. Future challenges include ensuring long-term operational stability and safety, as well as the safety of AAV injections for expressing light-sensitive proteins, such as GCaMP and ChrimsonR, in humans. As a long-term encapsulation material for medical use in optoelectronic semiconductor devices, Al_2O_3 films and their multilayer films produced by the atomic layer deposition (ALD) method are attracting attention as an alternative to parylene C [99], [100], [101]. Clinical trials have been conducted to express ChrimsonR in retinal cells using AAV injections [102], and advancements are anticipated alongside gene therapy progress [103].

Acknowledgments

This study was supported by JSPS KAKENHI (grant number: JP23H05450).

Conflicts of interests

Authors have no conflicts of interests to declare.

Ethical statement

This study was approved by the Nara Institute of Science and Technology Animal Experiment Ethics Committee (Animal Experimental Plan approval number: 2002; 1 April, 2020).

Authors' contribution

Yasumi Ohta: conceptualization, data curation, formal analysis, investigation, methodology, validation, visualization, writing—original draft. Virgil Christian Garcia Castillo: formal analysis, investigation, software. Romeo Rebusi Jr: investigation. Latiful Akbar: investigation. Joshua Philippe Olorocisimo: investigation. Austin Ganaway: investigation. Masahiro Ohsawa: funding acquisition, investigation, project administration, supervision. Yasemin M. Akay: project administration, supervision. Metin Akay: funding acquisition, project administration, supervision. Ryo Sasaki: investigation. Hirotaka Onoe: investigation. Kaoru Isa: investigation. Tadashi Isa: funding acquisition, project administration, supervision. Yoshinori Sunaga: investigation. Ryoma Okada: resources. Hironari Takehara: resources. Kiyotaka Sasagawa: supervision. Jun Ohta: funding acquisition, project administration, supervision, writing—review and editing.

References

[1] Chen T-W, Wardill TJ, Sun Y, Pulver SR, Renninger SL, *et al*. Ultrasensitive fluorescent proteins for imaging neuronal activity. *Nature* 2013, 499(7458):295-300.

[2] Deisseroth K. Optogenetics. *Nat Methods* 2011, 8(1):26–29.

[3] Haery L, Deverman BE, Matho KS, Cetin A, Woodard K, *et al.* Adeno-Associated Virus Technologies and Methods for Targeted Neuronal Manipulation. *Front Neuroanat* 2019, 13:93.

[4] Haggerty DL, Grecco GG, Reeves KC, Atwood B. Adeno-Associated Viral Vectors in Neuroscience Research. *Mol Ther Methods Clin Dev* 2019, 17:69–82.

[5] Ungerstedt U. Microdialysis--principles and applications for studies in animals and man. *J Intern Med* 1991, 230(4):365-373.

[6] Gunaydin LA, Grosenick L, Finkelstein J, Kauvar I, Fenno L, *et al.* Natural neural projection dynamics underlying social behavior. *Cell* 2014, 157(7):1535–1551.

[7] Simpson EH, Akam T, Patriarchi T, Blanco-Pozo M, Burgeno LM, *et al.* Lights, fiber, action! A primer on *in vivo* fiber photometry. *Neuron* 2024, 112(5):718–739.

[8] Ghosh KK, Burns LD, Cocker ED, Nimmerjahn A, Ziv Y, *et al.* Miniaturized integration of a fluorescence microscope. *Nat Methods* 2011, 8(10):871–878

[9] Miniscope. Available: http://miniscope.org/index.php/Main_Page (accessed on 9 February, 2025).

[10] Ohta J, Ohta Y, Takehara H, Noda T, Sasagawa K, *et al.* Implantable Microimaging Device for Observing Brain Activities of Rodents. *Proc IEEE* 2017, 105: 158–166.

[11] Choi J, Taal AJ, Meng WL, Pollmann EH, Stanton JW, *et al.* Fully Integrated Time-Gated 3D Fluorescence Imager for Deep Neural Imaging. *IEEE Trans Biomed Circuits Syst.* 2020,14(4):636–645.

[12] Ohta J. Implantable Optoelectronic Devices for Unified Early Diagnosis and Treatment: Toward Creation of Optoelectronic Pharmacolog. JP23H05450, Available: https://www.jsps.go.jp/file/storage/kaken_12_g726/r_5_en_23h05450.pdf (accessed on February, 2025).

[13] Kim M, Hong J, Kim J, Shin HJ. Fiber bundle-based integrated platform for wide-field fluorescence imaging and patterned optical stimulation for modulation of vasoconstriction in the deep brain of a living animal. *Biomed Opt Express* 2017, 8(6):2781–2795.

[14] Zubia J, Arrue J. Plastic Optical Fibers: An Introduction to Their Technological Processes and Applications. *Opt Fiber Tech* 2001, 7:101–140.

[15] Osanai M, Suzuki T, Tamura A, Yonemura T, Mori I, *et al.* Development of a micro-imaging probe for functional brain imaging. *Neurosci Res* 2013, 75(1):46–52.

[16] The Jackson Laboratory. Body Weight Information for B6 (000664) JAX® Mice Strain C57BL/6J, https://www.jax.org/jax-mice-and-services/strain-data-sheet-pages/body-weight-chart-000664# (accessed on February, 2025).

[17] LaManna JC, McCracken KA, Patil M, Prohaska OJ. Stimulus-activated changes in brain tissue temperature in the anesthetized rat. *Metab Brain Dis* 1989, 4(4):225–237.

[18] Dong N, Berlinguer-Palmini R, Soltan A, Ponon N, O'Neil A, *et al.* Opto-electro-thermal optimization of photonic probes for optogenetic neural stimulation. *J Biophotonics* 2018, 11(10):e201700358.

[19] Golda-Cepa M, Engvall, Minna Hakkarainen M, Kotarba A, Recent progress on parylene C polymer for biomedical applications: A review. *Progress in Organic Coatings* 2020, 140:105493.

[20] Rustami E, Sasagawa, Kenji Sugie K, Ohta Y, Haruta M, *et al.* Needle-Type Imager Sensor with Band-Pass Composite Emission Filter and Parallel Fiber-Coupled Laser Excitation. *IEEE Trans Circ Sys I* 2020, 67(4):1082–1091.

[21] Olorocisimo JP, Ohta Y, Regonia PR, Castillo VCG, Yoshimoto J, *et al.* Brain-implantable needle-type CMOS imaging device enables multi-layer dissection of seizure calcium dynamics in the hippocampus. *J Neural Eng* 2024, 17:21(4).

[22] Tanaka K, Choi YJ, Moriwaki Y, Hizawa T, Iwata T. Improvements of low-detection-limit filter-free fluorescence sensor developed by charge accumulation operation. *Jpn J Appl Phys* 2017, 56:04CM09.

[23] Deisseroth K, Feng G, Majewska AK, Miesenböck G, Ting A, Schnitzer MJ. Next-generation optical technologies for illuminating genetically targeted brain circuits. *J Neurosci* 2006, 26(41):10380–6.

[24] Klapoetke NC, Murata Y, Kim SS, Pulver SR, Birdsey-Benson A. Independent optical excitation of distinct neural populations. *Nat Methods* 2014, 11(3):338–46.

[25] Lanyi JK. Halorhodopsin, a light-driven electrogenic chloride-transport system. *Physiol Rev* 1990, 70(2):319-30.

[26] Chuong A, Miri M, Busskamp V, Acker L, Henninger M, *et al.* Minimally invasive optogenetic neural silencing. *Nat Neurosci* 2014, 85: 942–958.

[27] Tsakas A, Tselios C, Ampeliotis D, Politi C, Alexandropoulos D. Review of Optical Fiber Technologies for Optogenetics. *Results Opt* 2021 5:100168.

[28] Zorzos AN, Boyden ES, Fonstad CG. Multiwaveguide implantable probe for light delivery to sets of distributed brain targets. *Opt Lett* 2010, 35(24):4133–4135.

[29] Reddy JW, Lassiter M, Chamanzar M. Parylene photonics: a flexible, broadband optical waveguide platform with integrated micromirrors for biointerfaces. *Microsyst Nanoeng* 2020, 6:85–99.

[30] Ohta Y, Guinto MC, Tokuda T, Kawahara M, Haruta M, *et al.* Micro-LED Array- Based Photo-stimulation Devices for Optogenetics in Rat and Macaque Monkey Brains. *IEEE Access* 2021, 9:127937–127949.

[31] Ohta Y, Murakami TE, Kawahara M, Haruta M, Takehara H, *et al.* Investigating the Influence of GABA Neurons on Dopamine Neurons in the Ventral Tegmental Area Using Optogenetic Techniques. *Int J Mol Sci* 2022, 23(3):1114.

[32] Sekiguchi H. Development of MicroLED neuroscience probe. JSAP Rev 2023, 230421.

[33] Dehkhoda F, Soltan A, Ponon N, Jackson A, O'Neill A, Degenaar P. Self-sensing of temperature rises on light emitting diode based optrodes. *J Neural Eng* 2018, 15(2):026012.

[34] Wu F, Stark E, Ku PC, Wise KD, Buzsáki G, Yoon E. Monolithically Integrated μLEDs on Silicon Neural Probes for High-Resolution Optogenetic Studies in Behaving Animals. *Neuron* 2015, 88(6):1136–1148.

[35] Komatsu M, Sugano E, Tomita H, Fujii N. A Chronically Implantable Bidirectional Neural Interface for Non-human Primates. *Front Neurosci* 2017, 11:514.

[36] Sasaki R, Ohta Y, Onoe H, Yamaguchi R, Miyamoto T, *et al.* Balancing risk-return decisions by manipulating the mesofrontal circuits in primates. *Science* 2024, 383(6678):55–61.

[37] Rebusi R Jr, Olorocisimo JP, Briones J, Ohta Y, Haruta M, *et al.* Simultaneous CMOS-Based Imaging of Calcium Signaling of the Central Amygdala and the Dorsal Raphe Nucleus During Nociception in Freely Moving Mice. *Front Neurosci* 2021,15:667708.

[38] Akbar L, Castillo VCG, Olorocisimo JP, Ohta Y, Kawahara M, *et al.* Multi-Region Microdialysis Imaging Platform Revealed Dorsal Raphe Nucleus Calcium Signaling and Serotonin Dynamics during Nociceptive Pain. *Int J Mol Sci* 2023, 24(7):6654.

[39] Sunaga Y, Ohta Y, Murakami TE, M. Akay YM, Ohta J, *et al.* Monitoring Neural Activities in the VTA in Response to Nicotine Intake Using a Novel Implantable Microimaging Device. *IEEE Access* 2020, 8:68013–68020.

[40] Castillo VCG, Akbar L, Siwadamrongpong R, Ohta Y, Kawahara M, *et al.* Region of interest determination algorithm of lensless calcium imaging datasets. PLoS One 2024, 19(9):e0308573.

[41] Takehara H, Ohta Y, Motoyama M, Haruta M, Nagasaki M, *et al.* Intravital fluorescence imaging of mouse brain using implantable semiconductor devices and epi-illumination of biological tissue. *Biomed Opt Express* 2015, 6(5):1553–1564.

[42] Woolf CJ. What is this thing called pain? J Clin Invest 2010, 120: 3742–3744.

[43] Huang J, Zhang Z, Zamponi GW. Pain: Integration of Sensory and Affective Aspects of Pain. *Curr Biol* 2020, 30(9):R393–R395.

[44] Bushnell MC, Ceko M, Low LA. Cognitive and emotional control of pain and its disruption in chronic pain. *Nat Rev Neurosci* 2013, 14(7):502–11.

[45] Liu D, Hu SW, Wang D, Zhang Q, Zhang X, *et al.* An Ascending Excitatory Circuit from the Dorsal Raphe for Sensory Modulation of Pain. *J Neurosci* 2024, 44(4):e0869232023.

[46] Wilson TD, Valdivia S, Khan A, Ahn HS, Adke AP, *et al.* Dual and Opposing Functions of the Central Amyg dala in the Modulation of Pain. *Cell Rep* 2019, 29(2):332–346.e5.

[47] Ji G, Zhang W, Mahimainathan L, Narasimhan M, Kiritoshi T, *et al.* 5-HT2C receptor knockdown in the amygdala inhibits neuropathic pain-related plasticity and behaviors. *J. Neurosci* 2017, 37:1378–1393.

[48] Peyron C, Petit JM, Rampon C, Jouvet M, Luppi PH. Forebrain afferents to the rat dorsal raphe nucleus demonstrated by retrograde and anterograde tracing methods. *Neurosci* 1997, 82(2):443–468.

[49] Lopez-Alvarez VM, Puigdomenech M, Navarro X, Cobianchi S. Monoaminergic descending pathways contribute to modulation of neuropathic pain by increasing-intensity treadmill exercise after peripheral nerve injury. *Exp Neurol* 2018, 299: 42–55.

[50] Zhou W, Jin Y, Meng Q, Zhu X, Bai T, *et al.* A neural circuit for comorbid depressive symptoms in chronic pain. *Nat Neurosci* 2019, 22:1649–1658.

[51] Veinante P, Yalcin I, Barrot M. The amygdala between sensation and affect: a role in pain. *J Mol Psychiatry* 2013, 1(1):9.

[52] Paredes S, Cantillo S, Candido KD, Knezevic NN. An Association of Serotonin with Pain Disorders and Its Modulation by Estrogens. *Int J Mol Sci* 2019, 20(22):5729.

[53] Šimić G, Tkalčić M, Vukić V, Mulc D, Španić E, *et al.* Understanding Emotions: Origins and Roles of the Amygdala. *Biomolecules* 2021, 11(6):823.

[54] Neugebauer V, Li W, Bird GC, Han JS. The Amygdala and Persistent Pain. *Neuroscientist* 2004, 10: 221–234.

[55] Ressler KJ. Amygdala Activity, Fear, and Anxiety: Modulation by Stress. *Biol. Psychiatry* 2010, 67: 1117.

[56] Hamilton JP, Siemer M, Gotlib IH. Amygdala Volume in Major Depressive Disorder: A Meta-Analysis of Magnetic Resonance Imaging Studies. *Mol Psychiatry* 2008, 13:993–1000.

[57] Fuchs PN, Peng YB, Boyette-Davis JA, Uhelski ML. The anterior cingulate cortex and pain processing. *Front Integr Neurosci* 2014, 8:35.

[58] Shackman AJ, Salomons TV, Slagter HA, Fox AS, Winter JJ, *et al.* The integration of negative affect, pain and cognitive control in the cingulate cortex. *Nat Rev Neurosci* 2011, 12(3):154–67.

[59] Henry JL, Yashpal K, Pitcher GM, Chabot J, Coderre TJ. Evidence for tonic activation of NK-1 receptors during the second phase of the formalin test in the Rat. *J Neurosci* 1999, 19(15):6588-98.

[60] Lévesque M, Avoli M. The kainic acid model of temporal lobe epilepsy. *Neurosci Biobehav Rev* 2013, 37: 2887–99.

[61] Rusina E, Bernard C, Williamson A. The kainic acid models of temporal lobe epilepsy. *eNeuro* 2021, 8:1–24.

[62] Berdyyeva TK, Frady EP, Nassi JJ, Aluisio L, Cherkas Y, *et al.* Direct imaging of hippocampal epileptiform calcium motifs following kainic acid administration in freely behaving mice. *Front Neurosci* 2016, 10:53.

[63] Zhang X, Qiao Z, Liu N, Gao L, Wei L, *et al.* Stereotypical patterns of epileptiform calcium signal in hippocampal CA1, CA3, dentate gyrus and entorhinal cortex in freely moving mice. *Sci Rep* 2019, 9:4518.

[64] Naganuma K, Ohta Y, Murakami TE, Okada R, Guinto MC, *et al.* Multifunctional Implantable Device for Simultaneous Optical and Electrophysiological Measurements. *Sens Mat* 2022, 34(4):1561–1575.

[65] Sugie K, Sasagawa K, Okada R, Ohta Y, Takehara H, *et al.* Implantable multimodal sensing device for simultaneous imaging and electrophysiological recording of mouse brain activity. *Sens Mat* 2023, 35(9): 3173–3188.

[66] Castillo VCG, Tso K-C, Okada R, Ohta Y, Sunaga Y, *et al.* Laser-carbonized Electrodes on Implantable CMOS-based Imaging Device for Simultaneous Deep-brain Optical and Electrophysiological Measurements. *Sens Mat* 2024, 36(7):2735–2751.

[67] Kwan YCG, Ng GM, Huan CHA. Identification of functional groups and determination of carboxyl formation temperature in graphene oxide using the XPS O 1s spectrum. *Thin Solid Films* 2015, 590 :40–48.

[68] Aravanis AM, Wang LP, Zhang F, Meltzer LA, Mogri MZ, *et al.* An optical neural interface: In vivo control of rodent motor cortex with integrated fiberoptic and optogenetic technology. *J Neural Eng* 2007, 4(3):S143–S156.

[69] Roggan A, Minet O, Schroeder C, Mueller G. Determination of optical tissue properties with double integrating sphere technique and Monte Carlo simulations. *Proc SPIE* 1994. 2100:42–56.

[70] Mesradi M, Genoux A, Cuplov V, Abi Haidar D, Jan S, *et al.* Experimental and analytical comparative study of optical coefficient of fresh and frozen rat tissues. *J Biomed Opt* 2013, 18(11): 117010.

[71] Zubair M, Murris SR, Isa K, Onoe H, Koshimizu Y, *et al.* Divergent whole brain projections from the ventral midbrain in macaques. *Cerebral Cortex* 2021, 31(6):2913–2931.

[72] Huang S, Zhang Z, Gambeta E, Xu SC, Thomas C, *et al.* Dopamine inputs from the ventral tegmental area into the medial prefrontal cortex modulate neuropathic pain-associated behaviors in mice. *Cell Rep* 2020, 33(6):108393.

[73] Bass CE, Grinevich VP, Gioia D, Day-Brown JD, Bonin KD, *et al.* Optogenetic stimulation of VTA dopamine neurons reveals that tonic but not phasic patterns of dopamine transmission reduce ethanol self-administration. *Front Behav Neurosci* 2013, 7:173.

[74] Famm K, Litt B, Tracey KJ, Boyden ES, Slaoui M. Drug discovery: a jump-start for electroceuticals. *Nature* 2013, 496(7444):159–161.

[75] Chen WM, Chiueh H, Chen TJ, Ho CL, Jeng C, *et al.* A Fully Integrated 8-Channel Closed-Loop Neural-Prosthetic CMOS SoC for Real-Time Epileptic Seizure Control. *IEEE J Solid-State Cir* 2014, 49(1): 232–247.

[76] Volkow ND, Fowler JS, Wang GJ, Swanson JM. Dopamine in Drug Abuse and Addiction Results of Imaging Studies and Treatment Implications. *Arch Neuro* 2007, 64(11):1575–1579

[77] Everitt BJ, Robbins TW. Neural systems of reinforcement for drug addiction: From actions to habits to compulsion. *Nat Neurosci* 2005, 8(11):1481–1489.

[78] Patriarchi T, Cho JR, Merten K, Howe MW, Marley A, *et al.* Ultrafast neuronal imaging of dopamine dynamics with designed genetically encoded sensors. *Science* 2018, 360(6396): eaat4422.

[79] Ganaway A, Tatsuta K, Castillo VCG, Okada R, Sunaga Y, *et al.* Investigating the Influence of Morphine and Cocaine on the Mesolimbic Pathway Using a Novel Microimaging Platform. *Int J Mol Sci* 2023, 24(22):16303.

[80] Pathan H, Williams J. Basic opioid pharmacology: an update. *Br J Pain* 2012, 6(1):11–16.

[81] Siciliano CA, Jones SR. Cocaine Potency at the Dopamine Transporter Tracks Discrete Motivational States During Cocaine Self-Administration. *Neuropsychopharmacology* 2017, 42:1893–1904.

[82] Ohta Y, Murakami TE, Kawahara M, Haruta M, Takehara H, *et al.* Investigating the Influence of GABA Neurons on Dopamine Neurons in the Ventral Tegmental Area Using Optogenetic Techniques. *Int J Mol Sci* 2022, 23(3):1114.

[83] Johnston GA. Advantages of an antagonist: bicuculline and other GABA antagonists. *Br J Pharmacol* 2013, 169: 328–336.

[84] Wu N, Wan S, Su S, Huang H, Dou G, *et al.* Electrode materials for brain–machine interface: A review. *Info Mat* 2021, 3: 1174–1194.

[85] Roe AW. BMI 2.0: Toward a technological interface with brainwide networks. *Neuron* 2023, 111(11):1687–1688.

[86] Lebedev MA, Nicolelis MA. Brain-Machine Interfaces: From Basic Science to Neuroprostheses and Neurorehabilitation. *Physiol Rev* 2017, 97(2):767–837.

[87] Stauffer WR, Lak A, Schultz W. Dopamine Reward Prediction Error Responses Reflect Marginal Utility. *Curr Biol* 2014, 24(21): 2491–2500.

[88] Rudebeck PH, Saunders RC, Lundgren DA, Murray EA. Specialized Representations of Value in the Orbital and Ventrolateral Prefrontal Cortex: Desirability versus Availability of Outcomes. *Neuron* 2017, 95(5): 1208–1220.

[89] Yang E, Zwart MF, James B, Rubinov M, Wei Z, *et al.* A brainstem integrator for self-location memory and positional homeostasis in zebrafish. *Cell* 2022, 185 (26): 5011–5027.

[90] Deng F, Wan J, Li G, Dong H, Xia X, *et al.* Improved green and red GRAB sensors for monitoring spatiotemporal serotonin release *in vivo*. *Nat Methods* 2024, 21(4):692–702.
[91] Wang XY, Jia WB, Xu X, Chen R, Wang LB, *et al.* A glutamatergic DRN–VTA pathway modulates neuropathic pain and comorbid anhedonia-like behavior in mice. *Nat Commun* 2023, 14(1):5124.
[92] Song Q, Wei A, Xu H, Gu Y, Jiang Y, *et al.* An ACC–VTA–ACC positive-feedback loop mediates the persistence of neuropathic pain and emotional consequences. *Nat Neurosci* 2024, 27(2):272–285.
[93] Tan LL, Pelzer P, Heinl C, Tang W, Gangadharan V, *et al.* A pathway from midcingulate cortex to posterior insula gates nociceptive hypersensitivity. *Nat Neurosci* 2017, 20(11):1591–1601.
[94] Zhang Q, Hu S, Talay R, Xiao Z, Rosenberg D, *et al.* A prototype closed-loop brain–machine interface for the study and treatment of pain. *Nat Biomed Eng* 2023, 7(4):533–545.
[95] Sun G, Zeng F, McCartin M, Zhang Q, Xu H, *et al.* Closed-loop stimulation using amultiregion brain-machine interface has analgesic effects in rodents. *Sci Transl Med* 2022, 14(651): eabm5868.
[96] Takeuchi Y, Harangozó M, Pedraza L, Földi T, Kozák G, *et al.* Closed-loop stimulation of the medial septum terminates epileptic seizures. *Brain* 2021, 144(3):885-908.
[97] Müller C, Remy S. Septo–hippocampal interaction. *Cell Tissue Res* 2018, 373(3):565–575.
[98] Wang Y, Wang Y, Xu C, Wang S, Tan N, *et al.* Direct septum-hippocampal cholinergic circuit attenuates seizure through driving somatostatin inhibition. *Biol Psychiatry* 2020, 87(9):843–856.
[99] Carcia PF, McLean RS, Reilly MH, Groner MD, George SM. Ca test of Al2O3 gas diffusion barriers grown by atomic layer deposition on polymers. *Appl Phys Lett* 2006, 89:031915,.
[100] Xie X, Rieth L, Caldwell R, Diwekar M, Tathireddy P. Long-term bilayer encapsulation performance of atomic layer deposited Al_2O_3 and Parylene C for biomedical implantable devices. *IEEE Trans Biomed Eng* 2013, 60(10):2943–51.
[101] Abdulagatov AI, Yan Y, Cooper JR, Zhang Y, Gibbs ZM. Al2O3 and TiO2 Atomic Layer Deposition on Copper for Water Corrosion Resistance. *ACS Appl Mater Interface* 2011, 3:4593–4601.
[102] Sahel JA, Boulanger-Scemama E, Pagot C, Arleo A, Galluppi F, *et al.* Partial recovery of visual function in a blind patient after optogenetic therapy. *Nat Med* 2021, 27(7):1223–1229.
[103] Wirth T, Parker N, Ylä-Herttuala S. History of gene therapy. *Gene* 2013, 525(2):162–169.